JGR Solid Earth

RESEARCH ARTICLE
10.1029/2025JB032183

Structure of the North-Central Chile Subduction Zone From Local Earthquake Tomography

Nicolás Hernández-Soto[1,2], Christian Sippl[3], Matthew Miller[4], Dietrich Lange[5], Frederik Tilmann[6,7], Diego González-Vidal[4,8], Juan Carlos Baez[9], Anne Socquet[10], and Marcos Moreno[11]

[1]Departamento de Ciencias de la Tierra, Facultad de Ciencias Químicas, Universidad de Concepción, Concepción, Chile, [2]Escuela de Geología, Facultad de Ingeniería, Universidad Andrés Bello, Concepción, Chile, [3]Institute of Geophysics, Czech Academy of Sciences, Prague, Czechia, [4]Departamento de Geofísica, Facultad de Ciencias Fisicas y Matematicas, Universidad de Concepción, Concepción, Chile, [5]GEOMAR Helmholtz-Zentrum für Ozeanforschung Kiel, Dynamik des Ozeanbodens FE Marine Geodynamik, Kiel, Germany, [6]GFZ Helmholtz Centre for Geosciences, Potsdam, Germany, [7]Institut für Geologische Wissenschaften, Freie Universität Berlin, Berlin, Germany, [8]Proyecto de Monitoreo Volcánico de Alto Biobio, Universidad de Concepción, Concepción, Chile, [9]Centro Sismologico Nacional, Universidad de Chile, Santiago, Chile, [10]CNRS, IRD, ISTerre, Université Grenoble Alpes, University of Savoie Mont Blanc, University of Gustave Eiffel, Grenoble, France, [11]Departamento de Ingeniería Estructural y Geotécnica, Pontificia Universidad Católica de Chile, Santiago, Chile

Key Points:

- High-resolution tomography reveals elevated V_P/V_S ratios possibly linked to dehydration processes within the subducting Nazca Plate
- Double seismic zone, intermediate-depth seismicity and V_P/V_S anomalies around Copiapó Ridge suggest deeper slab hydration there
- V_P/V_S variations correlate with major crustal faults and mining zones linked to structural heterogeneity

Supporting Information:

Supporting Information may be found in the online version of this article.

Correspondence to:

N. Hernández-Soto,
nihernandez@udec.cl

Citation:

Hernández-Soto, N., Sippl, C., Miller, M., Lange, D., Tilmann, F., González-Vidal, D., et al. (2026). Structure of the North-Central Chile subduction zone from local earthquake tomography. *Journal of Geophysical Research: Solid Earth*, *131*, e2025JB032183. https://doi.org/10.1029/2025JB032183

Received 17 JUN 2025
Accepted 24 MAR 2026

Author Contributions:

Conceptualization: Nicolás Hernández-Soto, Christian Sippl, Dietrich Lange, Frederik Tilmann, Marcos Moreno
Data curation: Nicolás Hernández-Soto, Dietrich Lange, Diego González-Vidal
Formal analysis: Nicolás Hernández-Soto, Christian Sippl, Matthew Miller
Funding acquisition: Dietrich Lange, Frederik Tilmann, Juan Carlos Baez, Anne Socquet, Marcos Moreno
Investigation: Nicolás Hernández-Soto, Christian Sippl, Frederik Tilmann, Diego González-Vidal, Anne Socquet, Marcos Moreno
Methodology: Nicolás Hernández-Soto, Christian Sippl, Matthew Miller, Dietrich Lange, Diego González-Vidal

Abstract The fluid cycle in subduction zones prescribes large parts of its structure and seismogenic behavior. Background seismicity inside the downgoing slab is linked to fluid release from dehydration reactions, whereas fluid overpressure along the plate interface can alter interplate coupling, megathrust earthquakes, and the presence or absence of slow-slip events (SSEs) and tectonic tremor. We present a high-resolution seismic tomography model of the Atacama segment in northern Chile, the only region along the Chilean margin where SSEs have been observed. Using traveltimes from over 8,800 seismic events determined using state-of-the-art algorithms (EQTransformer, PyOcto), we followed a staggered workflow (VELEST, SIMUL2023) to derive consistent 1D, 2D and 3D models of P-wave velocity (V_P) and V_P/V_S ratios, achieving high spatial resolution in the upper continental crust, mantle, and downgoing slab. The final 3D model reveals key features interpreted as subsurface fluid processes. High V_P/V_S ($\geq$1.80) appears along the plate interface, with localized anomalies in the mantle wedge and lower continental crust. Regions with deep seismicity (~80–100 km depth), notably around the Copiapó Ridge, exhibit zones of higher V_P/V_S ratios ($\geq$1.82) extending upward from the oceanic slab into the continental crust, which otherwise shows lower V_P/V_S ratios ($\leq$1.76). These observations reflect along-strike variations in dehydration-driven fluid release accompanied by microseismicity. Liberated fluids ascend into the mantle wedge and updip along the slab surface, where they may influence SSEs. Our results provide new constraints on possible fluid pathways and crustal heterogeneity, highlighting the role of fluids in modulating seismogenic processes.

Plain Language Summary At the Atacama segment in North-Central Chile, a region that has not experienced a major earthquake in over 100 years, we detected 30,000 micro-earthquakes, many more than in previous studies, using over 100 seismic stations. By identifying seismic wave arrivals, we can image the Earth's lithosphere by creating a three-dimensional model of P- and S-wave velocities (V_P, V_S) and the V_P/V_S ratio. This helped us to uncover structures that influence seismic waves between the earthquake sources and seismic stations. Our findings show that fluids might infiltrate from the ocean into the oceanic Nazca Plate, where they are transported during subduction and released under certain conditions. This process generates seismicity at different depths. The presence of released fluids in the crust and mantle is interpreted by high V_P/V_S ratios. The fluids follow pathways seeking favorable conditions to move upward and accumulate, potentially triggering slow slip events (SSE), non-destructive slow aseismic slip at the plate interface, previously recorded around Copiapó. Additionally, we observed that the South American continental crust varies in thickness and structure from north to south, with fragmented areas that may be linked to ancient boundaries, which could facilitate fluid migration and contribute to the formation of shallow mineral deposits.

Project administration: Christian Sippl, Matthew Miller, Frederik Tilmann, Juan Carlos Baez, Anne Socquet, Marcos Moreno
Resources: Nicolás Hernández-Soto, Matthew Miller, Marcos Moreno
Software: Nicolás Hernández-Soto, Christian Sippl, Matthew Miller, Dietrich Lange, Diego González-Vidal
Supervision: Christian Sippl, Matthew Miller, Dietrich Lange, Frederik Tilmann, Anne Socquet, Marcos Moreno
Validation: Nicolás Hernández-Soto, Christian Sippl, Matthew Miller, Dietrich Lange
Visualization: Nicolás Hernández-Soto
Writing – original draft: Nicolás Hernández-Soto, Christian Sippl
Writing – review & editing: Nicolás Hernández-Soto, Christian Sippl, Matthew Miller, Dietrich Lange, Frederik Tilmann, Diego González-Vidal, Anne Socquet

1. Introduction

The circulation of fluids through the different parts of a subduction system are broadly considered as a major influence on the dynamics of the subduction zone (e.g., Faccenda, 2014). Water commonly enters oceanic plates at the mid-oceanic ridge as well as in the outer rise region of a subduction zone, where bend faulting leads to the opening of fluid pathways potentially deep into the lithospheric mantle (Ranero et al., 2003). Its infiltration leads to the formation of hydrous mineral phases that contain water bound in their crystal lattice, among them clay minerals such as smectite in sediments, amphiboles in the oceanic crust, or serpentines (lizardite, chrysotile, antigorite) in the oceanic mantle lithosphere (Faccenda, 2014). Upon subduction of the oceanic plate, these hydrous minerals gradually break down when exposed to increasing pressures and temperatures, thereby releasing the bound water. This occurs below the shallow plate interface for the water bound in subducting sediments, whereas the dehydration of oceanic crust and mantle extends to significantly larger depths (Rüpke et al., 2004), depending on the thermal state of the oceanic lithosphere (van Keken et al., 2011), and is considered to be linked to the occurrence of intermediate-depth seismicity (e.g., Peacock, 2001; Zhan, 2020).

Water that gets released below the plate interface is thought to accumulate there or to move upwards along the interface, as the entry into the upper plate is usually prevented by an impermeable seal (Husen & Kissling, 2001). This seal can, however, be fractured in places, for example, as the consequence of a large earthquake, allowing fluid ascent into the upper plate (Ma et al., 2022). Fluid presence along the plate interface is, together with fault unclamping (Scholz, 1998), thought to be directly linked to frictional heterogeneity, and thus possibly responsible for high fluid overpressure correlating with low interplate coupling (Moreno et al., 2014). Aseismic deformation as well as the occurrence of earthquake swarms have likewise been linked to regions of increased fluid presence along the megathrust (Marsan et al., 2023; Nishikawa & Ide, 2017). At depths below the seismogenic megathrust, fluids can enter the overlying mantle wedge, effecting the partial serpentinization of its cold outermost corner (Hyndman & Peacock, 2003). The large fluid volumes that get released from the deeper part of the slab rise through the hot mantle wedge, which leads to partial melting and contributes to the arc volcanism in the upper plate (Tatsumi, 1989).

As they link many important processes in active subduction zones, a more detailed mapping of fluid pathways and processes is essential for improving our understanding of subduction systems. One way to directly image fluids is via local earthquake tomography, where the ratio between P- and S-wave speeds (V_P/V_S) is highly sensitive to fluids (e.g., Christensen, 1996, 2004). High V_P/V_S values are thus conventionally interpreted as indicating the presence of fluids, whether as free aqueous fluids stored in pore and crack spaces, or structurally bound in hydrous minerals such as serpentine (e.g., Christensen, 2004; Hacker et al., 2003). In this study, we present a high-resolution local earthquake tomography study of North-Central Chile, using data from the first large-scale dense seismometer network in this region. The Atacama segment appears to be the only part of the Chilean margin where deep slow-slip events (SSEs), which are common in other subduction zones such as Cascadia or New Zealand (Schmalzle et al., 2014; Wallace, 2020), have been observed (Klein, Duputel, et al., 2018). As SSEs are commonly linked to fluid processes along the plate interface, understanding the fluid abundances and pathways in the Atacama segment may provide clues as to why SSEs occur here but have not been observed along the rest of the margin so far. Our results illuminate the distribution of fluids and their potential pathways in the region at higher resolution than previous studies, offering new cases of spatial correlation with the occurrence of intermediate-depth earthquakes, the influence of subducting seafloor features and the link between fluid processes and SSEs.

2. Study Area

The Atacama segment of the Chilean margin is delimited by the towns of Caleta El Cobre to the north and Tongoy to the south (Figure 1). Its large-scale tectonics are driven by the subduction of the Nazca plate under the South American plate at a rate of 65–67 mm/yr (Angermann et al., 1999). On the subducting Nazca plate, with age ranging from South to North from 40 to 50 Ma, two major bathymetric features, the Taltal Ridge (~25.5°S) in the north and the Copiapó Ridge (~27°S) further south, comprise discontinuous seamount chains, generated in an "off-ridge" hotspot setting (Bello-González et al., 2018). These seamount chains, with an estimated age of ~10 Ma (Bello-González et al., 2018), have been proposed to act as seismic barriers, playing a role in the segmentation of the margin (Contreras-Reyes & Carrizo, 2011; Molina et al., 2020; Sparkes et al., 2010). Both have been studied by amphibious refraction seismic imaging across the trench and down to ~25 km depth (Warwel,

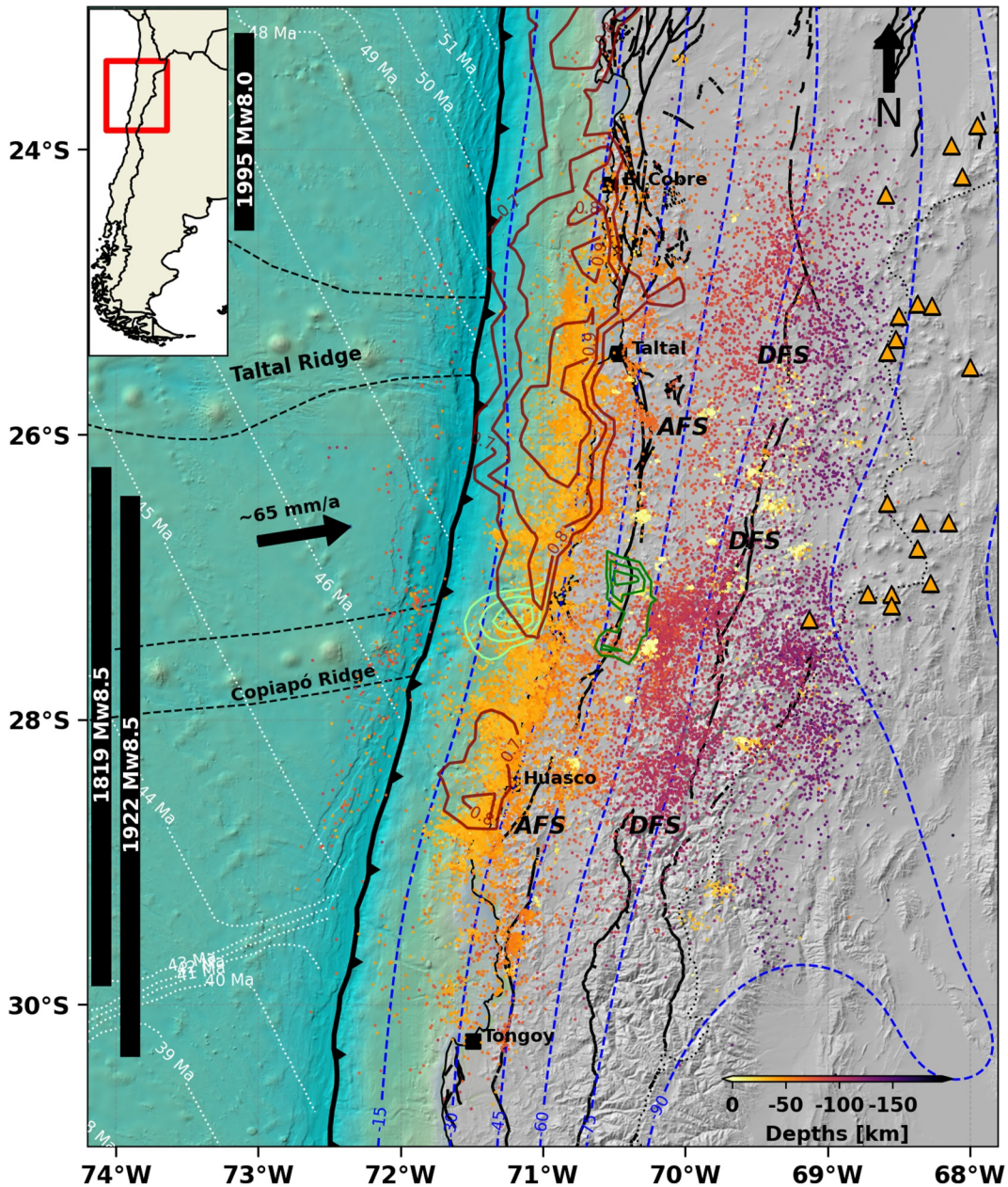

Figure 1. Tectonic setting of the study area. The colored dots indicate microseismicity as observed by González-Vidal et al. (2023); the shallow yellow clusters denote mining activity. The vertical black bars on the left show the estimated extent of historical earthquake ruptures (modified from Beck et al. (1998) and Ruiz and Madariaga (2018)). The traces of the Copiapó and Taltal Ridges are bounded by black dashed lines. Orange triangles represent the distribution of active volcanoes. The black barbed line offshore represents the trench, and the green dashed lines indicate depth contours of the slab surface from the SLAB2 model (Hayes et al., 2018). Black solid lines show fault systems mapped by Santibáñez et al. (2018), taken from Cortés-Aranda et al. (2022). The main traces of the Atacama Fault System and the Domeyko Fault System are referred to as AFS and DFS, respectively. Offshore dark red contours show highly locked (>0.7) regions after González-Vidal et al. (2023). Green contours around 27.5°S mark the slow slip event described by Klein, Duputel, et al. (2018). Light-green contours mark the 2023 shallow slow slip event described by Münchmeyer, Molina-Ormazabal, Radiguet, et al. (2025). Bathymetry and topography from GEBCO Bathymetric Compilation Group (2023). White dotted lines indicate sea-floor age isochrones at 1 Ma intervals from Müller et al. (2019) and Seton et al. (2020). Convergence vector from DeMets et al. (2010). The inset shows the location of the study area.

Lange, Dannowski, Contreras-Reyes, et al., 2025; Warwel, Lange, Dannowski, Klaucke, et al., 2025). The Copiapó Ridge is also the only site along the Chilean margin where repeating deep slow-slip events (SSE) have been detected (Klein, Duputel, et al., 2018). A first event observed in 2014 was followed by a recurrence in 2020 (Klein et al., 2021; Molina-Ormazabal et al., 2025), and additional studies have shown the presence of earthquake swarms in the region (Münchmeyer, Molina-Ormazabal, Radiguet, et al., 2025; Ojeda et al., 2023). At greater depths, the Nazca slab maintains a relatively shallow dip, gradually flattening toward the southern end of the Atacama segment, marking the transition into the Pampean Flat slab region (Ramos et al., 2002). The continental crust of the South American plate has a thickness of around 40 km in the forearc (Husen et al., 2000; Leon-Rios et al., 2024) and up to 60 km in the arc region (e.g., Álvarez et al., 2015), with a general tendency of thinner crust toward the south. The forearc basement in northern Chile is largely composed of Mesozoic volcanic and plutonic rocks, and associated Jurassic to Early Cretaceous granitoids, overlain by Cenozoic sedimentary sequences of limited thickness (Oliveros et al., 2007). Offshore, seismic and dredging data (e.g., Patzwahl et al., 1999; von Huene & Ranero, 2003) indicate that the sedimentary cover along the continental slope rarely exceeds 0.5 km, confirming a sediment-starved margin dominated by crystalline basement. This setting results from the extremely low input of terrigenous sediments into the trench, mainly due to long-term hyperarid conditions along the Atacama Desert (Kukowski & Oncken, 2006). Active crustal faults in the forearc are preferentially oriented N-S, and include the Atacama Fault System (AFS) to the west and Domeyko Fault System (DFS) in the eastern part of the forearc (Santibáñez et al., 2018).

Seismically, the Atacama segment of the Chilean margin in the southern part of our study region (26−30°S) is considered a major seismic gap, with the last megathrust $M_W \sim 8.5$ earthquake in 1922 (Beck et al., 1998; Ruiz & Madariaga, 2018; Vigny et al., 2024) (Figure 1). In the north, around 24°S, the 1995 M_w 8.0 Antofagasta earthquake (Ruegg et al., 1996) was the last major megathrust earthquake. Plate interface coupling maps derived from geodetic data show an overall highly locked plate interface in the region (González-Vidal et al., 2023; Klein, Metois, et al., 2018; Métois et al., 2014; Metois et al., 2016), highlighting the hazard potential of the segment. When considering smaller-scale seismicity, the Atacama segment appears as a region of low seismicity rates in national catalogs (Potin et al., 2025). However, this apparent low activity may, at least in part, reflect limitations in catalog resolution due to past station coverage. Recent results obtained from dense temporary deployments (e.g., González-Vidal et al., 2023; Münchmeyer, Molina-Ormazabal, Marsan, et al., 2025; Warwel, Lange, Dannowski, Contreras-Reyes, et al., 2025) have revealed tens of thousands of microearthquakes that remain undetected in routine national or global catalogs. Generally, seismicity in the upper crustal faults is scarce (Metcalf & Kapp, 2015), whereas large amounts of background seismicity are seen in the slab and along the plate interface. Swarm-like episodes of seismicity on the plate interface have been observed in 1973, 1976, 2006, 2020 (Comte et al., 2002; Holtkamp et al., 2011; Marsan et al., 2023; Münchmeyer, Molina-Ormazabal, Radiguet, et al., 2025; Ojeda et al., 2023) and were interpreted as the signature of aseismic processes related to the plate interface. In the same region, significant seismicity also occurs 20 km below the subduction interface, such as an M_W5.9 steep normal-faulting earthquake on 4 April 2023 (Warwel, Lange, Dannowski, Contreras-Reyes, et al., 2025); the mechanism of this earthquake could be related to slab pull or bending stresses in the upper part of the elastic slab lithosphere. Although double Benioff zones have been documented locally in northern Chile (Bloch et al., 2014; Dorbath et al., 2008; Sippl et al., 2018), such structures are generally not clearly resolved in routine global catalogs. So far, no systematic activity of low frequency earthquakes (LFEs) or tremors could be detected in the area (Münchmeyer, Frank, et al., 2025), except potentially, for a few isolated events (Pastén-Araya et al., 2022).

3. Methodology

3.1. Seismic Data

Our study area extends from ~24.5°S to 29.2°S and from ~72°W to 69°W. We used earthquake locations as well as P- and S-wave arrival times from an updated version of the catalog of González-Vidal et al. (2023), which contains a total of 33,748 events (Figure 1) composed of 507,037 P- and 458,002 S-wave picks. This catalog spans the time interval from November 2020 to December 2022, during which the ANILLO (Y6) (Tilmann et al., 2021) and ISTerre (XZ) (Socquet et al., 2020) temporary seismic networks were in operation. In addition, permanent stations from the national Chilean network (C, C1) (Universidad de Chile, 2012), the Integrated Plate Observatory Chile (GFZ German Research Centre For Geosciences & Institut Des Sciences De L'Univers-Centre National De La Recherche CNRS-INSU, 2006) and the GSN (Albuquerque Seismological Laboratory/USGS, 1988) were

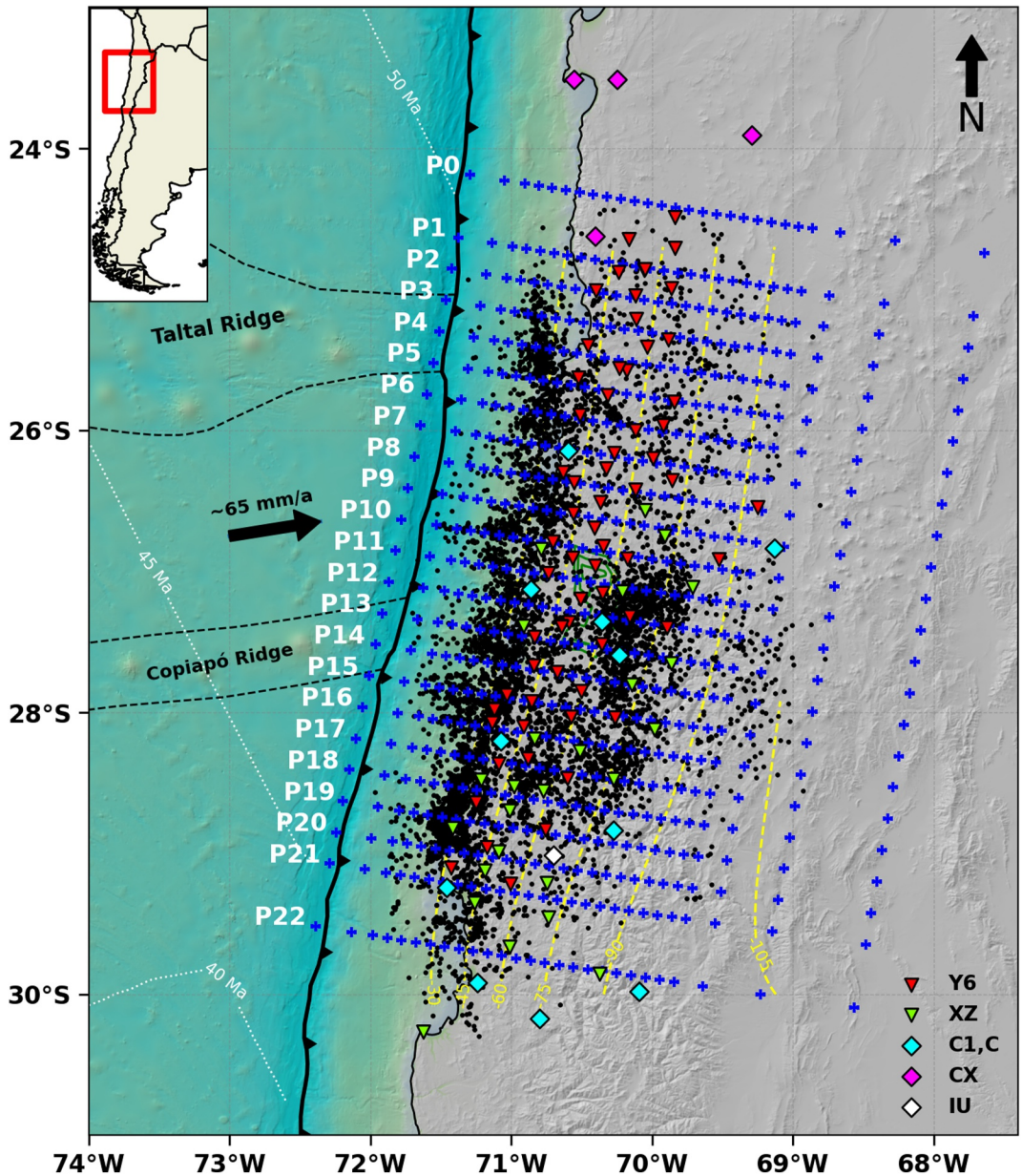

Figure 2. Topographic map showing the distribution of seismic stations and events selected for the tomographic inversion. Diamonds show permanent stations, and inverted triangles show temporary seismic stations. Black dots correspond to the selected events for the tomographic inversion. Blue crosses denote the grid nodes of the inversion, with the different profile names labeled in white. Bathymetry and topography from GEBCO Bathymetric Compilation Group (2023). White dotted lines indicate sea-floor age isochrones at 5 Ma intervals from Müller et al. (2019) and Seton et al. (2020). Convergence vector from DeMets et al. (2010).

used, leading to a dense coverage of the study area by a total of 104 seismic stations (see Figure 2). The catalog was obtained with an automated approach, using the deep learning-based phase picker EQTransformer (Mousavi et al., 2020), integrated in SeisBench (Münchmeyer et al., 2022; Woollam et al., 2022) and the phase associator PyOcto (Münchmeyer, 2024).

The data set that accompanies this publication represents a significant advance over previous seismological imaging efforts in the Atacama segment. Earlier tomographic studies in northern Chile relied on comparatively sparse permanent networks (e.g., Gao et al., 2025; Klein et al., 2021) or on regional-scale temporary deployments with limited density (e.g., Pastén-Araya et al., 2022). In contrast, our combination of dense temporary (Y6, XZ)

and permanent networks provides substantially improved spatial sampling across the forearc and slab. Specifically, the updated catalog used here builds upon González-Vidal et al. (2023) by extending the analysis period and by re-associating arrivals with PyOcto, whose superior performance relative to earlier associators has recently been demonstrated by Puente Huerta et al. (2025). As a result, our data set contains a significantly higher proportion of well-constrained P- and S-wave arrivals, leading to improved pick accuracy, event quality and quantity, and ray coverage. Additionally, our catalog complements that of Münchmeyer, Molina-Ormazabal, Marsan, et al. (2025), which focuses on the seismotectonic characterization of the Atacama segment. While both studies rely on a similar framework, our workflow is explicitly optimized for tomographic purposes, prioritizing pick accuracy, S-P differential times, and the selection of well-located earthquakes suitable for resolving 3D velocity structure. These advances provide a substantially enhanced and purpose-optimized foundation for high-resolution local earthquake tomography in the Atacama segment.

3.2. Tomographic Inversion

We followed a staggered approach to invert for subsurface wave speeds (see, e.g., Haberland et al., 2009; Sippl et al., 2013; Hicks et al., 2014; Lange et al., 2018). After an initial inversion for a minimum 1D model, we first inverted for V_P and V_P/V_S 2D models before obtaining the final 3D high-resolution model.

For retrieving the minimum 1D velocity model, we followed the strategy proposed by Kissling et al. (1994). The study volume was subdivided into small voxels outlined by 18 × 18 × 15 km in latitude, longitude, and depth, respectively, and then 984 candidate sources, distributed among the voxels, were selected based on the criteria of RMS residual <1.8 s, more than 20 arrival times (with at least 4 S picks), and an azimuthal gap smaller than 270°. Subsequently, starting from the 1D velocity model of Husen et al. (1999) and a homogeneous V_P/V_S ratio of 1.76 (Figure S1 in Supporting Information S1) estimated from analysis of the Wadati diagram, we simultaneously inverted for velocity model, hypocentral parameters and station corrections, obtaining an updated 1D velocity model using VELEST (Kissling et al., 1994). Following this, the hypocenters were relocated and a high-quality subset was retained, consisting of events meeting stricter criteria: RMS residual <0.15 s, more than 24 arrival times (with at least 8 S picks), and an azimuthal gap smaller than 240°. This selection, following the recommendation of Koulakov (2009), helped us retain high-quality events that provide valuable ray coverage and enhance path diversity, particularly from the western seismogenic zone and deep seismicity toward the less instrumented eastern side of our network, reaching the arc region. For a detailed view of the azimuthal distribution, refer to Figure S4 in Supporting Information S1. The relatively high azimuthal gap value improved our results by allowing the inclusion of valuable crossing rays from the shallow western and deeper eastern parts of the network, and achieve a more balanced sampling despite the asymmetric network geometry. The resulting raypath distribution can be observed in Figure S7 in Supporting Information S1. This resulted in a subset of 457 events distributed within the study volume, comprising 8,106 P-, and 6,814 S-wave arrival times, that were then used in a simultaneous inversion for the final minimum 1D V_P and V_P/V_S velocity models, hypocentral parameters and station corrections. All 33,748 events from the initial catalog were then relocated using this minimum 1D velocity model (Table S1 in Supporting Information S1). Although this model provides a large-scale average, it is predominantly representative of the upper-plate forearc domain, as this is the region with the highest raypath density, extending from the coastline to ∼150–180 km from the trench. To place our 1D velocity model in a broader context, we compare it with previously obtained velocity models along the Chilean subduction zone in Figure S33 in Supporting Information S1.

For the 2D and 3D inversions, a subset of 8,804 events was selected (A detailed description of the methodological procedure to obtain the 2D V_P and V_P/V_S models is provided in Text S2 of Supporting Information S1). These events include 193,050 P-wave and 135,438 S-wave arrival times. The events were filtered based on hypocentral parameters, selecting only those with RMS ≤ 1.5 s, more than 25 arrival times (with at least 10 being S-P differential times), and azimuthal gap smaller than 260°. Special attention was given to the sources, particularly near the trench and mining areas. Events close to the trench were excluded (only 15 events closer than 20 km), as well as those within a 20 km radius (and being shallower than 20 km) of recognized mining sites (obtained from Sociedad Nacional de Minería (2023)). The well-established code SIMUL2000 (Eberhart-Phillips & Michael, 1998; Thurber & Eberhart-Phillips, 1999) in its latest, updated version SIMUL2023 (Eberhart-Phillips et al., 2024) was used for 2D and 3D inversion. It uses the iterative damped least squares method to invert for the two- or three-dimensional velocity structure of V_P and V_P/V_S based on observed P- and differential S-P travel times, and employs a pseudo-bending ray tracing method (Um & Thurber, 1987) for the forward calculation of

travel times. In the 3D model, grid nodes are oriented perpendicular to the margin (Figure 2) along 23 profiles. Along each profile, the horizontal node spacing is 10 km across most of the study area, whereas the spacing between adjacent profiles is 25 km. Vertical spacing between grid nodes is 5 km at shallow depths (0–10 km), increasing to 10 km below 10 km depth and even larger values below 100 km depth. Using the 2D model as a starting model, the 3D inversion was first carried out for V_P only, with fixed V_P/V_S ratios. In a second run, V_P was then kept fixed, and V_P/V_S was inverted for. In both cases, the ideal choice of damping value was determined by the analysis of trade-off curves between data and model variance (Eberhart-Phillips, 1986; Haberland et al., 2009). Following the separate inversions, a final run, in which both V_P and V_P/V_S were allowed to vary simultaneously, was performed. In this step, station corrections were applied to improve the accuracy of the model. After 15 iterations of this last inversion, we achieved an overall RMS residual of 0.098 s, which is a reduction of 30.4% compared to the 2D model.

Finally, we conducted a two-step relocation process. Starting with the initial catalog, which had an RMS of 0.25 s, we first performed an absolute relocation of the entire earthquake catalog using the 3D model in SIMUL2023. This provided updated hypocenter locations that accounted for three-dimensional variations in seismic wave speeds, reducing the RMS to 0.12 s (a decrease of ∼51%). We then applied a relative relocation with hypoDD (version v2.1beta - 06/2012; Waldhauser and Ellsworth (2000)) using the minimum 1D velocity model. This relative relocation returned a RMS of 0.093 s for the double-difference residuals in the 1D model. The final relative hypocenters are shown in Figures 4 and 5.

4. Resolution Assessment

4.1. Checkerboard Tests

To evaluate the resolution capacity of the tomographic inversion, we conducted a range of synthetic tests. First, we ran standard checkerboard tests for both V_P and V_P/V_S with ±7.5% velocity perturbations over the depth range 10–100 km, with one checker encompassing either $1 \times 1 \times 1$ or $2 \times 1 \times 2$ grid nodes. The ±7.5% amplitude was selected because it reflects the order of magnitude of velocity contrasts expected in the area, such as those associated with upper-lower crustal variations and crustal-mantle transitions. Gaussian noise was added to the synthetic travel time data, with standard deviations ranging from 0.05 to 0.2 s, reflecting pick uncertainties defined by the quality classes in Table S2 in Supporting Information S1. We inverted the perturbed travel times employing the same procedure used to obtain our velocity models, which includes relocation of the seismic events at each inversion step.

For the checkerboard tests with $1 \times 1 \times 1$ anomalies (Figures S8–S11 in Supporting Information S1), the south-central region of the study area demonstrates better resolution, with the highest resolution for the V_P inversion observed in the central part at depths between 5 and 100 km. Laterally, the resolution remains good between 50 and 200 km from the trench. In contrast, the V_P/V_S ratios are considerably less well resolved across the entire study region. The resolved area covers depths between 5 and 80 km and extends laterally between 60 and 180 km from the trench. Strong smearing is evident outside of this region, due to limited ray coverage and sub-optimal receiver distribution, resulting in poor recovery of the initial checkerboard pattern.

Checkerboards with larger anomalies ($2 \times 1 \times 2$ nodes) yield improved results (see Figure 3. For a detailed view of all cross-sections and depth cuts, refer to Figures S12–S15 in Supporting Information S1). As in the previous test, the central and southern parts of the study area show the best-recovered regions. In these zones, the V_P inversion successfully retrieves anomalies down to depths of 115 km and laterally between 20 and 250 km from the trench (Figure 3, upper panels). For V_P/V_S ratios (Figure 3, lower panels), the well-recovered region extends laterally from ∼40–50 km to ∼220 km from the trench and reaches depths of up to 100 km.

To identify resolved regions for subsequent plots, we analyzed the correlation between the inversion results against the initial synthetic checkerboard patterns. Areas were classified as resolved based on the following three main criteria: (a) the recovered polarity matches that of the input model, (b) the recovered amplitude is greater than one-third of the original input amplitude, and (c) a final visual inspection to ensure consistency. If conditions (a) and (b) were met but the result appeared visually inconsistent, the amplitude threshold was increased to improve reliability. This combined approach ensured that only well-constrained regions were considered in the final interpretation. Nevertheless, even in areas classified as resolved, we exercised caution and avoided over-interpreting features near the borders of the resolved zones, where resolution typically degrades and artifacts such

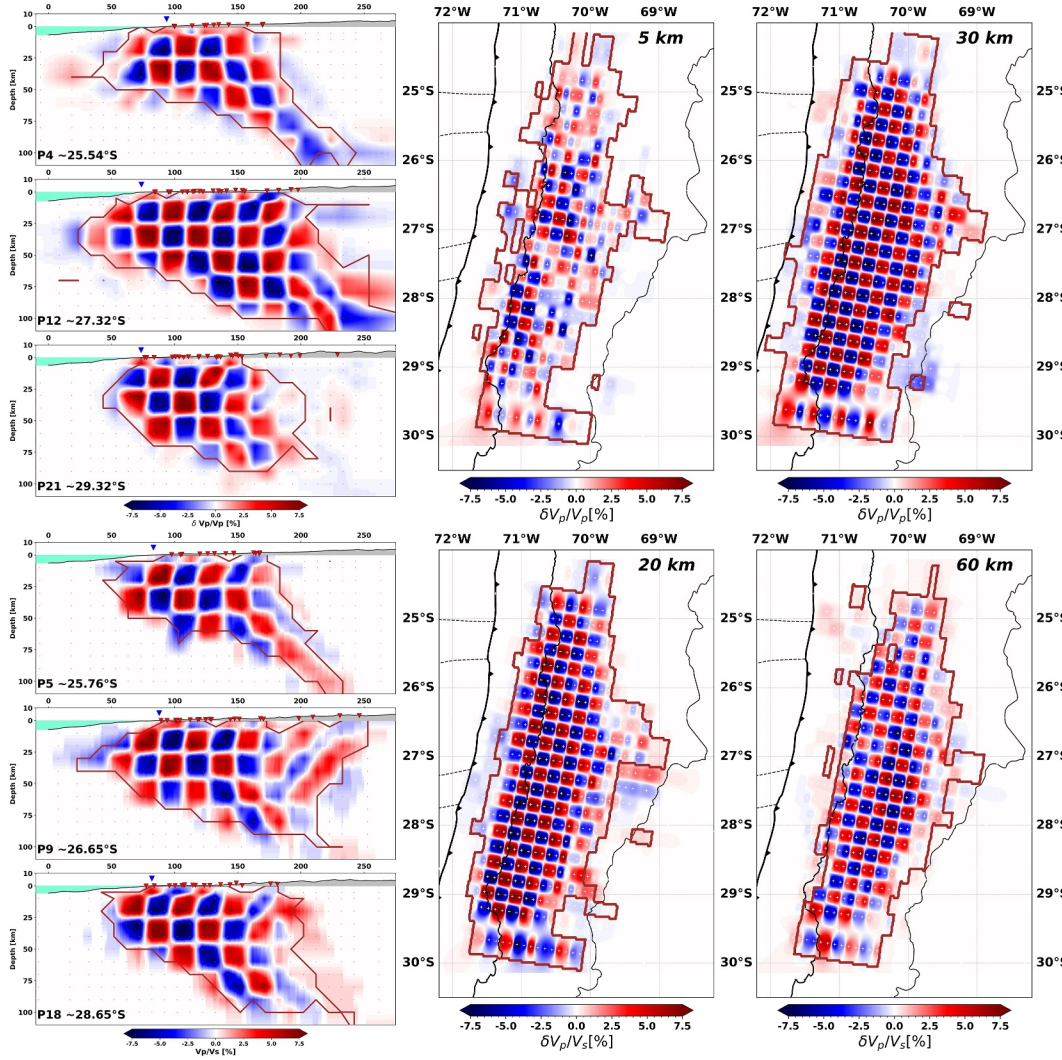

Figure 3. 3D synthetic checkerboard models with anomalies of $2 \times 1 \times 2$ node size for V_P (upper panels) and V_P/V_S (lower panels) inversions. Cross-sections are shown on the left; depth cuts (map view) on the right. Figures show the recovered structure from initial patterns with amplitudes of ±7.5%, for V_P and V_P/V_S ratios. The synthetic travel times were perturbed by adding random Gaussian noise with a standard deviation between 0.05 and 0.2 s, corresponding to the assigned quality levels for each pick. For cross-sections: The coastline is marked by an inverted blue triangle. Red inverted triangles indicate seismic stations. Topography from GEBCO. Black bottom labels indicate the profile and latitude. Maroon lines surround regions that are have sufficient resolution according to spread value threshold, see Section 4.2. For map views: Solid black lines denote the political border of Chile. White crosses mark the node distribution. Upper black label indicates the depth. All other cross-sections and map views are shown in Figures S8–S15 in Supporting Information S1.

as smearing may occur. As a consequence of this resolution assessment, we mainly analyze and interpret features that correspond to the size of the $2 \times 1 \times 2$ checkerboards in this study.

4.2. Spread Values

Additionally, we evaluated the spatial resolution of the inversion using the Spread Function of the resolution matrix (SF; e.g., Toomey & Foulger, 1989), which quantifies the compactness of the averaging kernels around each node. The corresponding SF values for both the V_P and V_P/V_S models are shown in Figures S16–S19 in Supporting Information S1 in cross-sections and iso-depth map views, where lower spread values indicate better-resolved regions.

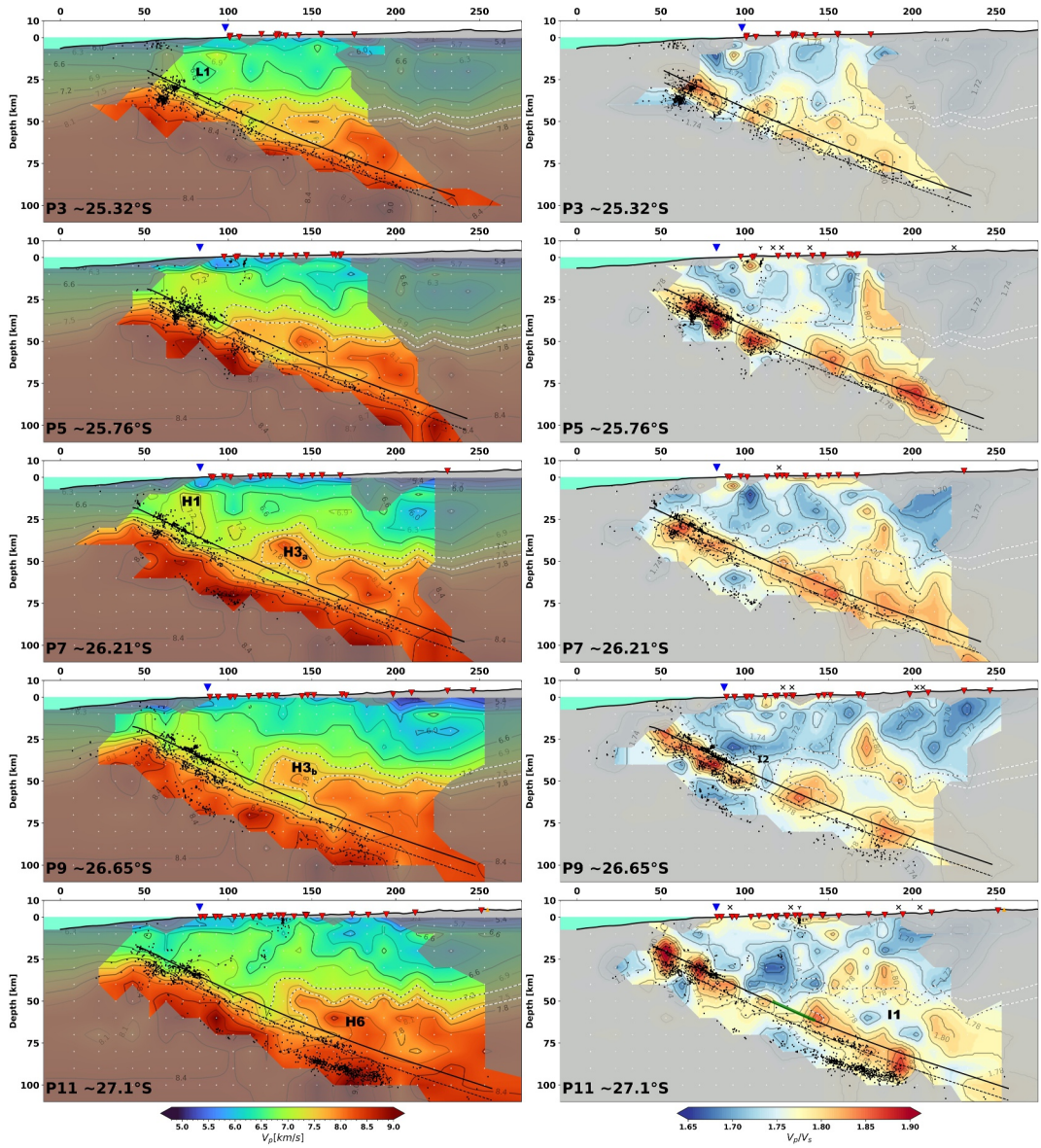

Figure 4. 3D velocity model plotted along five cross-sections (northern part), sorted from north to south. For each profile, the profile label code (as in Figure 2) and latitude at the center of each profile are found in the bottom left corner. Regions with low resolution according to spread values higher than 3.5 (see Section 4; Figures S8–S19 in Supporting Information S1) are shaded. The coastline location is denoted by the inverted blue triangle. Topobathymetry from GEBCO. The red inverted triangles represent seismic stations within a 100 km-wide swath window (±50 km for each profile). Black dots depict the final relocations of the seismicity within a 25 km swath window around the profile. Black solid line represents our proposed slab surface model (see Text S1 and Figure S27 in Supporting Information S1). The dashed black line marks the ∼7 km-thick oceanic crust beneath the slab surface. Black and white dashed lines delineates the continental seismic Moho proxy, corresponding to the vertical gradient in which P-wave speeds increase from 7.2 to 7.6 km/s. The green line in P11 V_P/V_S profile (and P13 in the next figure) represents the location of the SSE (Klein, Duputel, et al., 2018) along the proposed interplate contact. The black "Y"s mark known mining operations, black crosses indicate surface traces of crustal faults (Santibáñez et al., 2018). Black labels denote high or low anomalies. Anomalies assigned the same number but differentiated by subscripts (e.g., $H3_a$, and $H3_b$) indicate laterally extensive features across multiple profiles.

A threshold of 3.5 for the spread values was selected to discriminate between regions with high and low resolution, and the spread value is now superimposed on all velocity models. The threshold was carefully determined based on the consistency between the checkerboard recovery patterns (Figure 3 and Figures S8–S15 in Supporting Information S1), the ray coverage distribution (Figures S7, S20, and S21 in Supporting Information S1), and the

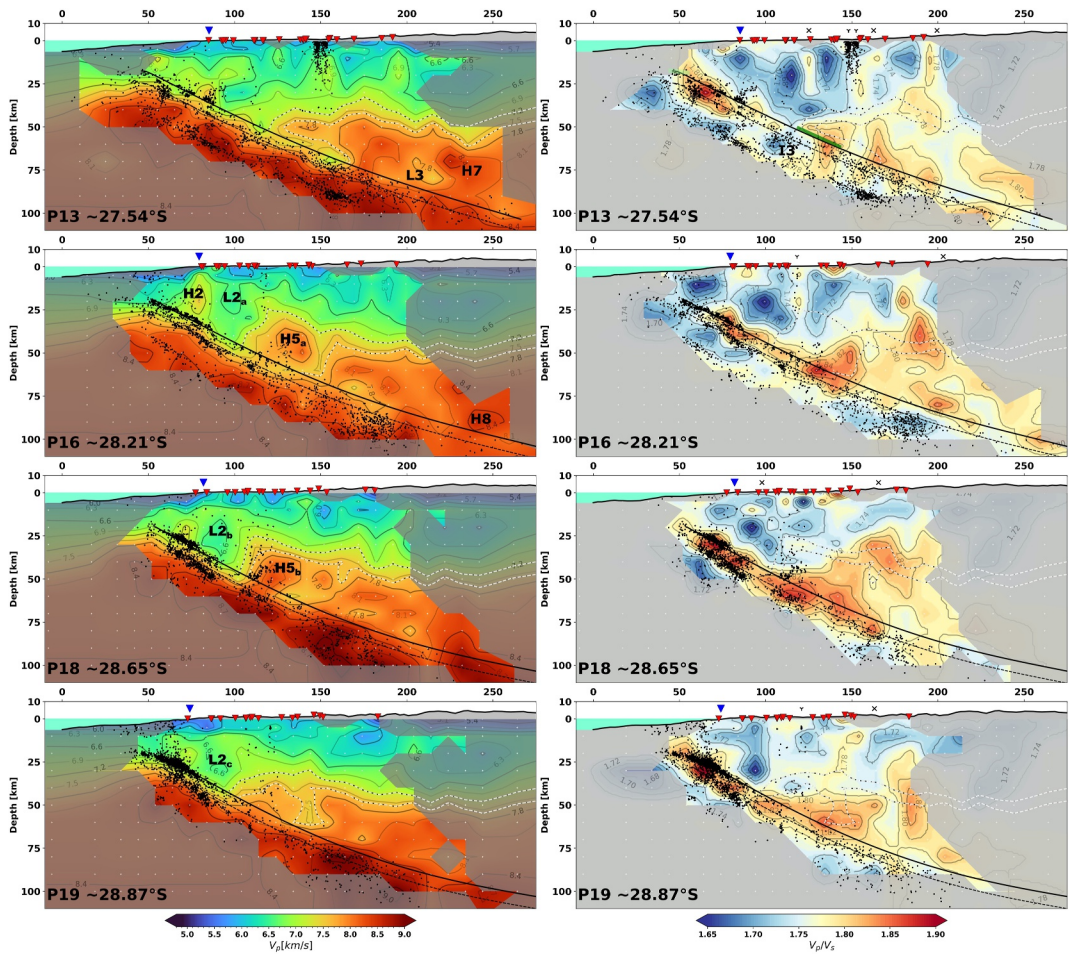

Figure 5. 3D velocity model plotted along four cross-sections (southern part). The light green line in Profile P13 (and Profile P12 in Figure S26 in Supporting Information S1) represents the location of the 2023 Shallow SSE (Münchmeyer, Molina-Ormazabal, Radiguet, et al., 2025) along the proposed interplate contact. All other plot features as described in the caption of Figure 4.

spread value (Figures S16–S19 in Supporting Information S1). This conservative but robust criterion was applied to mask poorly constrained areas (in gray), ensuring that only features within the well-resolved area are interpreted and discussed.

5. Results

The retrieved three-dimensional velocity models (V_P and V_P/V_S) are presented as margin-perpendicular cross-section plots along nine profiles in Figures 4 and 5. The final relocated seismicity is displayed together with the velocity structure. We will first describe our findings for the downgoing plate, including the plate interface region, then move on to the upper plate.

5.1. Downgoing Plate and Plate Interface Region

The subducting oceanic plate is imaged from a starting depth of ~20 km and exhibits an uppermost layer characterized by crustal V_P values (~6.9–7.5 km/s), with a vertical thickness of 5–10 km (Figures 4 and 5). It is present to a depth of ~60 km at all profiles, and disappears or thins at larger depths, especially in the north. Its V_P values are largely indistinguishable from the overlying continental crust, whereas a sharp velocity jump occurs at the oceanic Moho, where V_P quickly increases to >7.8 km/s and then gradually increases with depth. This thickness is consistent with the expected depth of ~7 km below the plate interface reported by Warwel, Lange, Dannowski, Contreras-Reyes, et al. (2025) and Warwel, Lange, Dannowski, Klaucke, et al. (2025). Accordingly,

at depths of <50 km, the 7.5 km/s iso-velocity contour (dashed black line in Figures 4 and 5) best approximates the slab Moho. The velocity structure of this crustal layer is consistent with the subducting oceanic crust imaged to depths of up to ∼25 km by Warwel, Lange, Dannowski, Contreras-Reyes, et al. (2025) and Warwel, Lange, Dannowski, Klaucke, et al. (2025) near Copiapó and Taltal. Their velocity models show a comparable thickness; however, they resolve lower V_P (3.5–6.5 km/s) values for a ∼2 km-thick oceanic upper crust, whereas our model predominantly images higher velocities (6.9–7.5 km/s), that are more representative of the oceanic lower crust. This difference likely reflects the resolution limit of our model and, potentially, the onset of metamorphic transformations at depths >25 km. The deepening and lateral variations of this oceanic crustal feature are well resolved in our 3D model due to the dense ray coverage, providing additional constraints at depths ≥40–50 km, which are not well resolved by Warwel, Lange, Dannowski, Contreras-Reyes, et al. (2025) and Warwel, Lange, Dannowski, Klaucke, et al. (2025). At these depths, our results reveal a heterogeneous oceanic mantle characterized by isolated patches with $V_P \geq 8.0$ km/s, which may be consistent with relatively dense mantle lithologies such as peridotites (Christensen, 1996; W. Mooney, 2007). Although these heterogeneities may represent new observations for the Atacama segment and could suggest along-strike and along-dip variations in the physical properties of the subducting mantle, they should be interpreted with caution. In particular, the influence of deeper less well-resolved nodes, together with locally limited resolution, may affect the recovery of such velocities. Further investigation would therefore be required to better constrain the physical properties of the oceanic mantle beneath the Atacama segment.

V_P/V_S ratios show, to first order, a similar behavior, with high V_P/V_S (≥1.78) in the uppermost part of the downgoing slab and substantially lower V_P/V_S (≤1.74) in deeper parts of the slab. For reference, typical V_P/V_S values are ∼1.79–1.89 for oceanic crust, and ∼1.77–1.84 for oceanic mantle (Christensen, 1996; Graeber & Asch, 1999; Hacker et al., 2003). However, in our model, the high-V_P/V_S layer appears to extend deeper into the slab (thickness of up to 20 km) than the low P-wavespeeds, and it does not thin or disappear toward greater depths. This layer exhibits considerable heterogeneity, with localized V_P/V_S peaks (∼1.84–1.88) observed between 30 and 40 km depth, sometimes as deep as 60–70 km (Profiles P5, P7, P11, P18).

The two-years-long recorded seismicity along and inside the downgoing plate defines two to three planes that are parallel to the slab's dip, predominantly situated between 50 and 200 km from the trench (Figures 4 and 5). A first alignment of seismicity is prominent along the plate interface at depths of 20–40 km, and will be named hereafter the interplate seismicity plane. At approximately 7–8 km below the plate interface, a second alignment of seismicity is apparent. This second plane concentrates most of its activity directly beneath where the plate interface seismicity is present, but also extends to greater depths, although events are less numerous there. A third, deeper plane of seismicity occurs at ≥20 km below the plate interface. It is only present in some profiles (e.g., Profiles 7, 9, 11, 13, 16), and is most visible at depths >70 km. The ∼20 km spacing between the shallowest and deepest planes is consistent with the Double Benioff Zone configuration for a ∼45 Ma subducting plate described by Brudzinski et al. (2007) and further documented by Sippl et al. (2018), confirming recent observations by Warwel, Lange, Dannowski, Contreras-Reyes, et al. (2025). A detailed comparison with previous observations in and around the Atacama segment is provided in Text S3 of Supporting Information S1.

It is interesting to note that seismicity concentrations are generally surrounded by high-V_P/V_S regions, particularly along the plate interface. Moreover, the second seismicity plane, which corresponds to the upper plane of the double seismic zone, seems to be situated in the vicinity of the oceanic Moho.

5.2. Continental Crust and Mantle Wedge

In the continental crust, V_P values generally increase with depth from the surface toward the continental Moho. The lowest V_P values (≤6.0 km/s) are found in the uppermost 5 km, where localized anomalies of $V_P \leq 5.4$ km/s are primarily observed offshore (e.g., Profiles P9 to P19) or toward the eastern end of the study region (∼200 km from the trench; Profiles P9, P11). Isolated patches of high V_P/V_S ratios (≥1.78) are also common in this shallowest layer, particularly around ∼150 km from the trench, exceeding the typical V_P/V_S values of ∼1.72–1.77 expected for continental crust (Christensen, 1996; W. D. Mooney et al., 2025). They sometimes coincide with notable clusters of shallow seismicity (e.g., Profiles P11 and P13, approximately 135 and 150 km from the trench) that stem from regions of high mining activity.

Within ∼50 km landward from the trench, in the shallower parts of the upper plate, high-V_P/V_S ratios locally extend upward from the plate interface into the offshore marine forearc crust (e.g., Profiles P11–P13 in Figures 4

and 5). These anomalies occur updip of the shallow interplate seismicity and indicate that elevated V_P/V_S values are not restricted to the downgoing oceanic slab but locally penetrate the overriding plate.

At mid-crustal depths (15–30 km; e.g. W. D. Mooney et al., 2023), high P-wavespeeds of ≥7 km/s are found at relatively shallow depths beneath the coastline and offshore (H1, and H2 in Profiles P7 and P16, respectively). In contrast, V_P values decrease toward the east, down to 30–40 km depth south of P5 (at 200 km from the trench), where the continental crust is characterized by significantly slower velocities ($V_P \leq 6.5$ km/s). Several isolated low-V_P anomalies are also found along the coastline (L1, L2a, L2b, and L2c in Profiles P3, P16, P18, P19, respectively), where V_P/V_S ratios remain low throughout the crust (<1.76). Onshore, high-V_P anomalies are found at depths of 40–60 km, often ∼5–7.5 km above the lower (downdip) part of the plate interface background seismicity (H3a, H3b, H5a, and H5b in Profiles P7, P9, P16, P18, respectively; V_P7.8–8.2 km/s). These high-V_P anomalies are co-located with patches of high V_P/V_S ratios (≥1.78) that appear to protrude a few kilometers into the continental crust from the plate interface region, but do not have the same vertical extent as the high V_P anomalies. Toward the eastern end of the well-resolved region, high-V_P/V_S areas extend further upwards into the continental crust. These high-V_P/V_S zones appear more prominent and homogeneous in the southern profiles (Profiles P16, P18, P19) and occasionally extend to shallow depths (≤10 km; Profiles P5, P13, P16). In Profile P18, within this depth range, a distinct high-velocity region (H5b) is present, which connects to high-V_P features within the oceanic slab and shows a strong correlation with seismicity rising from the plate interface to the overriding plate.

We defined a zone bounding the plausible depth of the continental seismic Moho using the 7.2 and 7.6 km/s isocontours, indicated with white/black dashed lines in Figures 4 and 5. These contours correspond to the center of the strongest vertical velocity gradients at the base of the continental crust and provide upper and lower bounds of a plausible Moho proxy, thereby avoiding reliance on a single fixed velocity threshold in our tomographic model. The sub-horizontal continental Moho is thus between 40 and 50 km depth east of ∼150 km from the trench. Where it intersects with the plate interface, it is situated significantly deeper, generally around ∼55–60 km depth in the central profiles (P8–P14), while this intersection tends to occur slightly shallower in the southernmost and northernmost profiles (∼42–45 km depth). Interestingly, in these central profiles, the vertical gradient is markedly wider, in contrast with the nearly parallel boundaries that otherwise define the boundaries of plausible continental Moho. Even when these depths locally exceed the average crustal thickness of ∼40 km aforementioned, they likely reflect lateral variations in the composition and structure of the crust-mantle boundary. One possible explanation is that the continental Moho lies closer to the shallower bound of this interval, while comparatively lower V_P values in the uppermost mantle result in a broader crust-mantle transition. Such variations may be influenced by the subducted seamounts of the Copiapó Ridge, which could locally distort the crust-mantle boundary.

Lastly, localized high-V_P anomalies (≥8.3 km/s) are observed in Profiles P11, P13, and P16 (H6, H7, and H8, respectively), along with low-V_P zones (7.5–7.8 km/s) that exhibit a heterogeneous structure at greater depths, particularly in the south-central areas. These low-V_P regions are usually found in close vicinity to the plate interface. At depths greater than 50 km, high V_P/V_S values extend from the plate interface in a more pervasive way into the mantle wedge. The V_P/V_S ratios in the upper mantle are consistently higher than in shallower areas, ranging from 1.78 to localized peak values of ∼1.84. The only exception is Profile P11 (I1), where isolated low V_P/V_S ratios (≤1.74) are located between 60 and 70 km depth.

6. Discussion

In order to interpret our observations, we derived a new local slab surface geometry model by fitting a polynomial surface to the relocated seismicity catalog, in a manner similar to Sippl et al. (2018). This new slab model, which shows major differences from SLAB2 (Hayes et al., 2018) in some locations at depths beyond the megathrust, is shown in our profile plots in Figures 4 and 5, together with a parallel line 7 km below that represents the approximate location of the oceanic Moho for an assumed normal oceanic crust. For a detailed comparison between our proposed slab geometry model, "NewSlab," and the SLAB2 model, please refer to Supporting Information S1, specifically Text S1 and Figure S27 in Supporting Information S1.

6.1. Imaging of the Oceanic Crust and Its Eclogitization

Absolute V_P values reveal a ∼7–8 km thick layer with V_P ∼ 6.7–7.4 km/s at the top of the downgoing oceanic plate (Figures 4 and 5). The geometry of the interplate contact as well as the inferred oceanic Moho at depths of ∼20–25 km along our Profiles P13–P14 and P3–P4 is broadly consistent with the active-source seismic results of

Warwel, Lange, Dannowski, Contreras-Reyes, et al. (2025) and Warwel, Lange, Dannowski, Klaucke, et al. (2025), except for the shallowest offshore portion, where our resolution is limited. The observed thickness is consistent with the expected total thickness of normal oceanic crust. However, in contrast to the active-source results of Warwel, Lange, Dannowski, Contreras-Reyes, et al. (2025) and Warwel, Lange, Dannowski, Klaucke, et al. (2025), which resolve a ∼2 km-thick low-velocity upper oceanic crust overlying a faster lower crust, our local earthquake tomography does not resolve this internal subdivision. Instead, the imaged velocities are dominated by values typical of lower oceanic crust, representing the upper bound of gabbroic velocities above the Moho (e.g., Christeson et al., 2019; Grevemeyer et al., 2018), and compare well with offshore seismic results to the north of the study area (e.g., Ranero & Sallarès, 2004; Sallarès & Ranero, 2005). We interpret the absence of a distinct low V_P upper-crustal layer in our model primarily as a consequence of the limited vertical resolution of our local earthquake tomography. Moreover, these velocities are also consistent with the constraints on the oceanic lower crust derived from recent active-source seismic experiments conducted directly within the study area. Locally, slight reductions in V_P (down to ∼6.7 km/s) may instead result from fracturing associated with pervasive plate bending. At depths of 70–100 km, the thin layer likely representing the oceanic crust disappears, and is replaced with material of $V_P \geq 8$ km/s, similar to the oceanic mantle lithosphere below. The depth where this occurs appears to become shallower toward the south (Figures 4 and 5). We interpret this observation as evidence for the eclogitization of the basaltic and gabbroic rocks of the oceanic crust due to having been subducted into the pressure-temperature conditions of the eclogite stability field. Eclogite features seismic wavespeeds highly similar to mantle lithospheric peridotite (e.g., Worthington et al., 2013), which often leads to the disappearance of the oceanic Moho in receiver function images. However, we note that the vertical node spacing of 10 km in our 3D model may limit our ability to resolve a thin remnant layer of oceanic crust only a few kilometers thick that has not yet undergone complete eclogitization. In Yuan et al. (2000), for instance, the oceanic Moho of the downgoing Nazca Plate vanishes at ∼120 km depth in their profile situated at about 24.5°S, consistent with our observed trend of northward deepening of this transition. In our northernmost profile, situated about 100 km further south, velocities at the downdip edge of resolution (∼95 km depth) have not reached values above 8.0 km/s, which may indicate that the completion of the basalt/gabbro to eclogite transition is located deeper. Similarly, Garth and Rietbrock (2017) demonstrated further north at ∼23°S that a ∼1 km-thick low-velocity layer, interpreted as un-eclogitized oceanic crust, may persist to depths of at least 220 km, suggesting that crustal transformation along northern Chile could be progressive and may extend well beyond the depths resolved in our model.

6.2. Dehydration Reactions and Intermediate-Depth Intraslab Seismicity

The top of the downgoing Nazca Plate also shows elevated V_P/V_S ratios (≥1.8), down to depths of 70–90 km, which usually occur in the uppermost 10–15 km of the slab. At 50 km depth, the region of high V_P/V_S is thicker than the low-V_P layer at the slab top. It extends into the forearc crust of the upper plate, as well as into the mantle wedge at depths greater than 50 km, and does not vanish with depth (Figures 4 and 5). We thus interpret this widespread high V_P/V_S anomaly as the presence of fluids that get expelled from hydrated minerals in the oceanic crust and mantle lithosphere when these minerals undergo phase transitions. Such processes have been associated with the generation of intermediate-depth intraslab seismicity (e.g., Hacker et al., 2003; Peacock, 2001; Zhan, 2020). Our observation that the shallower band of intraslab earthquakes is situated in a high-V_P/V_S environment (≥1.8), whereas the lower band is surrounded by rather low V_P/V_S values (∼1.72–1.78), is highly similar to the findings of Tsuji et al. (2008) in NE Japan. In most of the central profiles (P5–P13), the high-V_P/V_S regions around the slab top exhibit their maximum values at shallow depths (20–50 km) as well as at depths ≥70 km, with an area of weaker or no elevated V_P/V_S in-between. Intriguingly, this high V_P/V_S distribution pattern corresponds at first order to regions of highest earthquake density within the shallower band of intraslab seismicity. The shallow intraslab events, located around the oceanic Moho, occur directly beneath the plate interface seismicity and align with the lower edge of the shallow high-V_P/V_S regions. Similarly, the deeper intraslab seismicity is visible directly below the deeper high-V_P/V_S region in several profiles (Profiles P9, P11, P13). As fluids released within the oceanic crust and sub-Moho mantle lithosphere are expected to rise (sub) vertically along high-permeability pathways due to their buoyancy, we interpret these oceanic intra-crustal high-V_P/V_S regions as a result of dehydration reactions. These reactions, indicated by the presence of intraslab seismicity, result in fluid release and ascent (shown by the elevated V_P/V_S ratios). The different regions of seismogenesis at different depths could be due to dehydration reactions occurring first in the oceanic crust, and

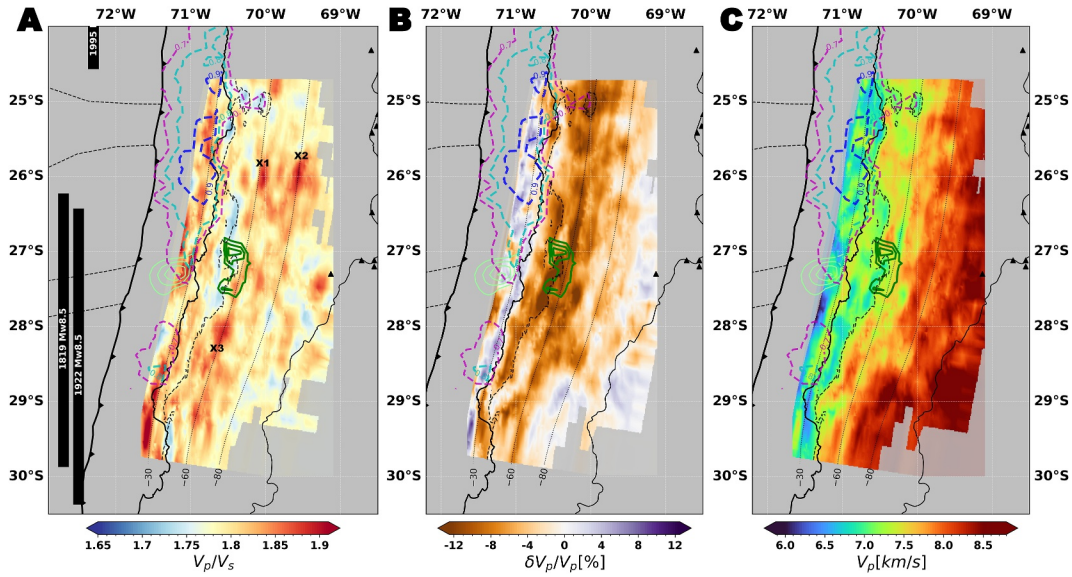

Figure 6. Features along the interplate contact. (a) V_P/V_S ratios. (b) Relative V_P variation with respect to the 1D velocity model. (c) V_P values (km/s). Magenta, cyan, and blue contours indicate zones of high interplate coupling (≥0.7) as estimated by González-Vidal et al. (2023). The slip distribution of the 2014 Slow Slip Event (Klein, Duputel, et al., 2018) is represented by +7.5 cm green contour lines (starting from 20 cm). The north-to-south black dashed line marks the intersection between the plate interface and the continental Moho (inferred from $V_P \sim 7.2$ km/s, which represents the upper limit of our selected plausible continental Moho). Black dashed lines offshore represent the Taltal and Copiapó Ridges. Black triangles denote nearby active volcanoes. Black solid lines indicate the political borders of Chile. Black bars represent past large earthquakes from 1. Interplate iso-baths at 30, 60 and 80 km are marked with North-to-south dashed lines.

subsequently activating dehydration in the oceanic mantle lithosphere at greater depths, as previously proposed by Rüpke et al. (2004).

A prominent and persistent north-to-south band of intermediate-depth seismicity is observed deep inside the slab at and around where the Copiapó Ridge is subducted (Profiles P10 to P13). Subducting oceanic features like ridges or fracture zones can often be delineated as narrow zones of increased intraslab seismicity (e.g., Geersen et al., 2022; Kirby et al., 1996), which is likely because they feature anomalously fractured oceanic crust and upper mantle through which more fluids than elsewhere can enter to deeper intraslab depths at the outer rise. Offshore Copiapó, Warwel, Lange, Dannowski, Contreras-Reyes, et al. (2025) observed bending-related faults visible in the bathymetry and reduced mantle velocities near the trench, suggesting the presence of mantle hydration. The lower plane of double seismic zone seismicity is commonly linked to the dehydration reaction of serpentinite, which occurs around 600–650°C (e.g., Peacock, 2001), although some authors doubt whether the hydration of the downgoing plate can penetrate to such depths (Korenaga, 2017). If we assume that lower plane seismicity is linked to serpentinite dehydration, then the presence or absence of seismicity at deep intraslab depths likely depends on whether hydration at the outer rise extends sufficiently deep in these locations. This could explain our observation of increased levels of intermediate-depth earthquakes, most of them situated in the deeper part of the slab, along the projected trace of the subducting Copiapó Ridge (see also Figure 7). At those depths within the mantle, fluids released by dehydration reactions would not necessarily migrate freely through the entire thickness of the oceanic mantle. Instead, they may be redistributed along localized permeable pathways and could partly be trapped within the overlying mantle, where serpentinization may still be active under temperatures below ∼600°C. It is surprising that the Taltal Ridge further north does not show a similar signature. We can only speculate that this may be due to different faulting patterns or structural conditions, or that the Taltal Ridge could be discontinuous in its already subducted part.

6.3. Properties and Fluid Processes Along the Plate Interface and the Downgoing Slab

The plate interface is characterized by a widespread presence of high V_P/V_S ratios (≥1.78) across most of its extent which complements the observations made by Grevemeyer et al. (2018) to greater depths (Figure 6a).

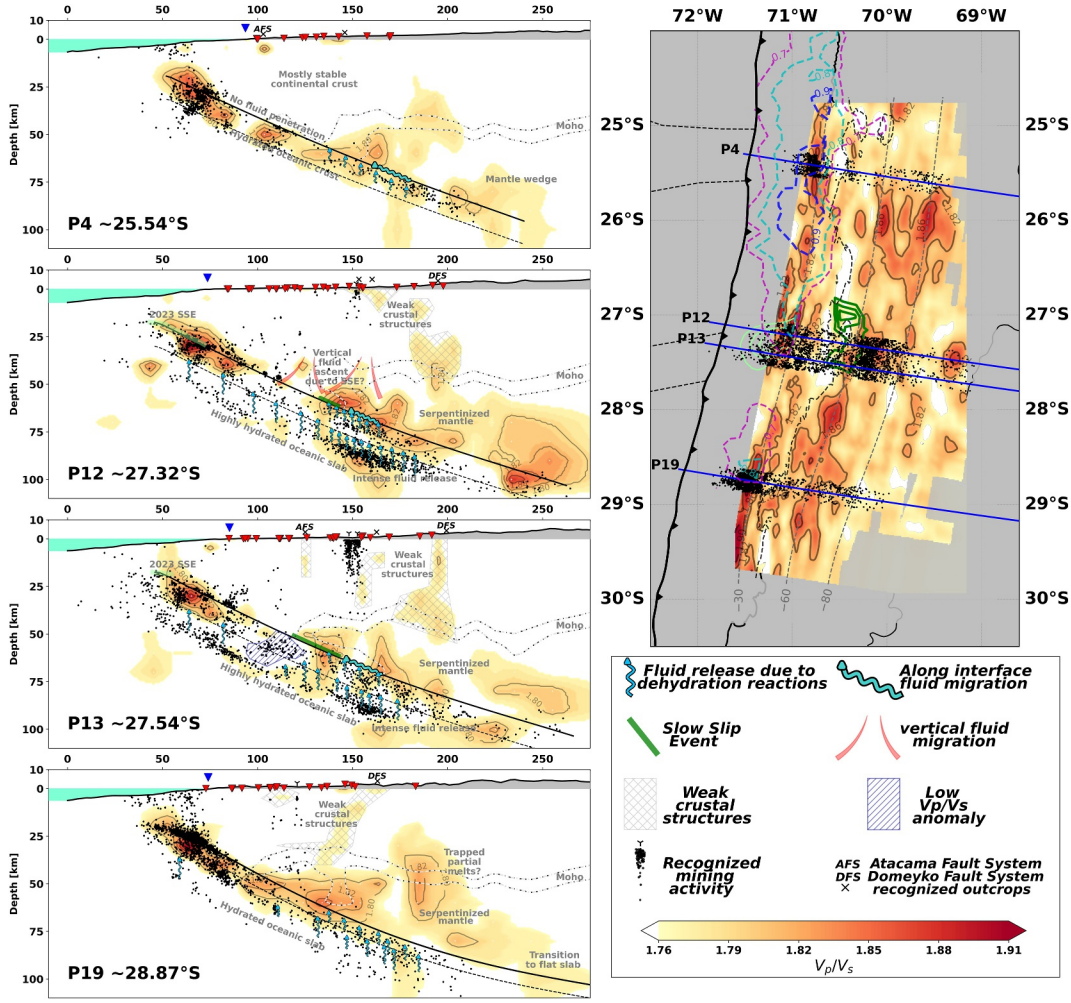

Figure 7. Schematic summary of the main observations and interpretations for key profiles (left panels) of the study area (map in the upper right corner). The left panels present interpretations from top to bottom: North (Profile P4), the Copiapó Ridge (Profiles P12 and P13), and South (Profile P19), emphasizing prominent north-to-south variations. The map view on the right presents the profiles locations (blue lines). Areas of elevated V_P/V_S ratios (≥1.82) are delineated by contours. Iso-depth contours at 30, 60, and 80 km are indicated by dashed gray lines. The black dashed north-to-south line denotes the inferred mantle wedge corner. Black dots in each cross-section correspond to hypocenters also shown in the map view. In cross-sections, intense fluid release is represented by thin light-blue wavy arrows, while thick light-blue wavy arrows indicate zones of fluid migration along the slab interface. Fluid accumulation zones are indicated by warm colors according to the accompanying color scale. SSE areas are shown in green (thick lines in the profiles and contours in the map view). Light-green contours mark the 2023 shallow slow slip event described by Münchmeyer, Molina-Ormazabal, Radiguet, et al. (2025). The Atacama Fault System (AFS), Domeyko Fault System (DFS), and other minor fault outcrops compiled by Santibáñez et al. (2018) are marked with black "x" symbols. Zones of enhanced mining activity are indicated by black "Y" symbols.

Localized patches with even higher values (≥1.82) are commonly observed in the updip region along the crustal contact between the two plates (shallower than 30 km depth). Notably, deeper zones with elevated V_P/V_S ratios are identified at around 60 km depth south of 28°S, and near 60 and 80 km depth around 26°S (labeled as X1, X2, and X3 in Figure 6a). We interpret the high V_P/V_S ratios in the updip region as indicative of the release of fluids from the underlying oceanic crust. These fluids likely originate from the breakdown of clay minerals and hydrous minerals in the crust that are expected to be pervasive down to Moho depths due to plate bending processes occurring seawards of the trench. This is consistent with the well-established process of fluid release at shallow depths in subduction zones, and with previous observations along the Northern Chilean margin (e.g., Husen et al., 2000; Pastén-Araya et al., 2018). However, these elevated V_P/V_S areas are not continuous along strike but instead appear segmented. Such segmentation may reflect along-strike variations in several key elements, including the composition of the oceanic crust and of the Copiapó and Taltal ridges and associated seamounts,

variations in fabric orientation, associated rheology and degree of fracturing, and the pressure-temperature regime. These along-strike variations can modify the thermal structure and the depth or efficiency of dehydration, with cooler segments delaying dehydration or shifting it downdip. Additionally, fluid ascent and migration are unlikely to be uniform; fluids may preferentially migrate through mechanically weaker zones such as bending-related faults, subduction-interface roughness associated with seamount subduction, or lithologic boundaries that act as transient fluid traps. The physical properties of the upper-plate forearc crust, including its lithology and degree of fracturing, may further influence whether fluids are able to drain upward into the overriding plate or instead remain trapped along the plate interface. These factors can collectively produce the observed laterally discontinuous high V_P/V_S patches.

The deeper zones of elevated V_P/V_S ratios along the interplate contact at depths greater than 60 km may reflect the accumulation of fluids derived from dehydration processes occurring inside the downgoing plate. This process may be associated with the progressive or complete eclogitization of the oceanic crust, with these fluids subsequently migrating upward and pooling along the slab top and above. Notably, some of these anomalies (e.g., X1 and X2 in Figure 6a) do not coincide clearly with subducted oceanic features. However, this apparent mismatch may partly reflect uncertainties in the expected subsurface location of the Copiapó and Taltal ridges, which have been interpreted as continuous structures extending for more than 200 beyond the trench, as well as their change in strike near the trench (Bello-González et al., 2018). This spatial pattern suggests that the along-strike variability of fluid accumulation is controlled not only by the geometry of the subducted ridges, but also by variations in the permeability structure of both plates, which can modulate the efficiency of fluid transport from the lower crust and sub-Moho mantle to the interface. As a result, fluids may become stored or focused in specific subsegments, even away from discrete incoming-plate structures. The upward migration of these fluids may be driven by buoyancy forces along mechanically favorable pathways such as zones of contrasting permeability (Barnes et al., 2010; Wang et al., 2019). Consistent with this interpretation, fluid accumulation appears to occur along the interplate contact downdip of ∼60 km depth (Figure 7, Profiles P4, P12 and P13), below the continental Moho (Koulakov et al., 2006; Yuan et al., 2000). A deeper zone of high V_P/V_S ratios, centered at ∼80 km depth and in places connected to the 60 km depth anomaly, is observed around 26°S (Figure 7, upper right corner (map view)). While fluid accumulation alone may explain these elevated V_P/V_S values, the spatial extent and vertical distribution to the shallow crust in at least some of our profiles, suggest that it likely reflects metamorphic fluid release during eclogitization of the downgoing slab. These fluids may migrate upward along the slab surface and into the overlying mantle wedge, where they could contribute to rheological weakening and, at shallower depths, facilitate partial melting beneath the volcanic arc.

When comparing the resulting velocity models with the interseismic locking model proposed by González-Vidal et al. (2023) (Figure 6), we observe a spatial relationship that varies significantly depending on whether along-dip or along-strike changes are considered.

For V_P/V_S ratios (Figure 6a), no clear large-scale along-strike relationship is observed with the degree of coupling. This could suggest that, at least within this segment, fluid presence and interplate locking are not simply related, a finding similar to observations in South-Central Chile (Hicks et al., 2014). However, along-dip, an apparent spatial relationship emerges. Around 25.8°S, 27.1°S, and 28.8°S, the downdip termination of highly locked patches (≥0.8) coincides with zones of elevated V_P/V_S ratios (≥1.84), similar to findings of Moreno et al. (2014) further south. This could suggest a possible control of high V_P/V_S ratios on the downdip limit of locking at the Atacama segment. Alternatively, this relationship may operate in the opposite direction; the downdip limit of the locked Atacama segment could in turn influence fluid distribution and accumulation, both beneath the overriding crust and further downdip along the plate interface, potentially contributing to the observed V_P/V_S structure. Regarding V_P anomalies (Figure 6b), a clearer along-dip pattern is evident: areas of positive ΔV_P correlate with areas of stronger locking (≥0.8), while negative ΔV_P anomalies tend to mark the downdip transition to lower coupling values (≤0.7). Similarly, when absolute V_P values are considered (Figure 6c), several structures of intermediate-to-low V_P values (≤6.8 km/s) also appear to modulate the downdip extent of high coupling (≥0.7), which is particularly pronounced in the southernmost high-locking patch, south of 28°S.

In contrast, the along-strike correlation between V_P/V_S and coupling is less clear. A localized low V_P/V_S anomaly near 28°S coincides with a subsegment of relatively low coupling (<0.7) between two strongly coupled areas (≥0.7). However, elevated V_P/V_S values extend farther south beyond 29–30°S despite the marked reduction in locking. This behavior is consistent with observations by Kodaira et al. (2004), who showed that elevated pore-

fluid pressures inferred from high Poisson's ratio (and thus high V_P/V_S) can expand zones of stable or conditionally stable slip within otherwise strongly coupled segments, complicating any simple along-strike relationship between V_P/V_S and locking. Finally, this southern extension of high V_P/V_S lies largely offshore, where resolution is low, further limiting interpretations. The relative (respect to the minimum 1D model, see Figures S28 and S29 in Supporting Information S1) and absolute V_P values (Figures 6b and 6c, respectively) exhibit a more coherent along-strike relationship with locking. As noted earlier, positive ΔV_P anomalies tend to spatially correlate with zones of high coupling, while zones of negative ΔV_P anomalies are prevalent in areas of lower locking ($\leq$0.7). For absolute V_P values, highly coupled zones ($\geq$0.7) are clearly separated by a region of low V_P ($\leq$6.8 km/s), with the lowest V_P values ($\leq$6.4 km/s) located offshore of 27.8°S, coinciding with an along-strike segmentation of high-locking contours ($\geq$0.7).

These observations suggest that zones of reduced plate locking, potentially due to fluid presence or compositional heterogeneity, have a signature in our tomographic images (e.g., Mishra et al., 2003; Pastén-Araya et al., 2022).

The area hosting the 2023 shallow SSE coincides with high V_P/V_S ratios ($\geq$1.82), which locally extend upward from the plate interface into the overlying forearc crust (see Profiles P11, P12, P13 in Figures 4, 5, and 7, and the map views shown in Figure 6). Although this area lies close to the limits of tomographic resolution, such elevated ratios may suggest increased damage and fluid-rich conditions within the forearc crust than elsewhere. Farther downdip, the deep recurrent Slow Slip Events (SSE) region (Klein et al., 2023; Klein, Duputel, et al., 2018; Molina-Ormazabal et al., 2025) is characterized by sparse seismicity (Warwel, Lange, Dannowski, Contreras-Reyes, et al., 2025), relatively low V_P in the overlying continental material (crust or mantle, depending on the local Moho depth), and by high V_P/V_S ratios ($\geq$1.78) along most of its downdip extent (Profiles P11 in Figure 4 and P13 in Figure 5, as well as Profile P12 in Figure 7 and Profile P10 in Figure S26 in Supporting Information S1). These elevated ratios coincide with the area where gravity anomalies suggest the presence of a subducted seamount near 27.55°S (Molina-Ormazabal et al., 2025), which also corresponds to the region where the 2020 SSE initiated. Farther north, where the aseismic slip propagated, the V_P/V_S values are lower (Profile P11 in Figure 4; Profile P13 in Figure 5; see also Figure 7, upper right). In contrast, Profile P13 reveals a localized break in the otherwise continuous high-V_P/V_S signature of the upper downgoing plate-expressed as a low-V_P/V_S anomaly ($\leq$1.74; label I3 in Figure 5, P13)-situated below the depth at which the SSEs are inferred to occur. Additional synthetic tests incorporating this scenario confirm that the observed low-V_P/V_S disruption within the surrounding high-V_P/V_S slab is well resolved and not an artifact of limited resolution or smearing (Figures S22–S24 in Supporting Information S1).

At first glance, a low-V_P/V_S anomaly co-located with where SSEs occur appears counter-intuitive, as these processes are commonly linked to fluid processes (Kato et al., 2010; Shelly et al., 2006). A plausible hypothesis is that the low V_P/V_S we observe corresponds to a localized, intraslab region where the oceanic crust is already dehydrated, producing a comparatively dry volume at ~60 km depth within the slab. Because this feature is confined to the slab interior, it does not contradict the fluid-rich conditions inferred along the megathrust in the southern sector of the SSE. In this region, mechanical damage and permeability contrasts induced by bending-related faults and the subducted Copiapó seamount (Molina-Ormazabal et al., 2025), together with upper-plate damage, may facilitate the drainage of fluids (Warwel, Lange, Dannowski, Contreras-Reyes, et al., 2025). These processes could also promote heterogeneous fluid redistribution and may generate an anomalous high-density zone consistent with the observed positive residual gravity anomaly (Molina-Ormazabal et al., 2025). At even greater depths, the upwelling of fluids likely have a mantle source, and hence would not be affected (see Figure 7, Profiles P12 and P13).

Alternatively, the low V_P/V_S ratio observed in Profile P13 could represent a doming structure associated with the subduction of seamounts, as previously described in the area by Pastén-Araya et al. (2022). Such a structure could be affecting fluid pathways, for example, by preventing along-slab fluid ascent into the low-V_P/V_S region. Recurrent SSEs may also promote upward (sub-vertically and along-dip) fluid migration, progressively depleting fluid content in their source region (see Figure 7, Profiles P12 and P13). This depletion could be part of an "inter-SSE" period, during which fluid recharge and pore pressure build-up are hypothesized to occur (Nakajima & Uchida, 2018). In addition, the relatively deep position of the plausible Moho in the central segment may indicate either a locally thicker crust or mantle wedge domain with $V_P < 7.2$ km/s. In the first case, elevated temperatures ($T > 350$°C) may promote aseismic slip along the interface, whereas in the second case fluids and temperatures

below ∼600°C could favor serpentinization of the mantle wedge, which has been proposed to facilitate SSE behavior.

While these scenarios provide plausible explanations for the observed low-V_P/V_S anomaly present along the updip limit of the SSE, they do not fully explain the occurrence of SSEs in a region that appears to lack abundant fluids. An alternative hypothesis can be drawn from the mechanism proposed for shallow SSEs at the Hikurangi margin, where weak, clay-rich volcaniclastic materials have been proposed to promote slow slip even under limited fluid availability (Barnes et al., 2020; Gase et al., 2023; Shreedharan et al., 2022, 2023). Although no comparable volcaniclastic material has been documented in our study area, subducting seamounts can contain altered volcanic material rich in hydrous minerals, including clays, which may influence megathrust mechanical behavior (Molina-Ormazabal et al., 2025). If similar altered materials are present within the subducted seamounts of the Copiapó Ridge, they could offer an additional source of mechanical weakening along the interface. This suggest that other, yet unidentified factors may also facilitate slow slip in this environment.

6.4. Fluid Migration Into the Upper Plate

From the analysis of V_P and V_P/V_S ratios, we observe significant north-to-south variations in the continental crust. In the northern part of the study area (∼24.4°S–∼26.6°S), particularly along profiles P1–P9 and within ∼150–200 km landward from the trench, the crust is predominantly characterized by moderate-to-low V_P/V_S ratios (≤1.75), and high V_P/V_S ratios are largely absent above the plate interface contact. This suggests that fluids do not significantly migrate into the overlying continental crust, possibly due to insufficient permeability in its basal structure, or because the high locking degree may be sealing the plate interface, thereby preventing fluid circulation along the interface and their upward propagation into the upper plate (Figure 7, Profile P4). Our continental Moho estimate shows that crustal thickness ranges between 30 and 50 km, consistent with published studies (Koulakov et al., 2006; Sodoudi et al., 2011; Tassara & Echaurren, 2012; Yuan et al., 2000). This thickness, together with the predominance of low to moderate V_P/V_S ratios (≤1.75) in the northern part of the study area, suggests a generally dense, cold, and stable felsic lithology for the upper-plate crust. Toward the south, however, the distribution of low V_P/V_S ratios (≤1.74) becomes markedly more heterogeneous, confined to small, discontinuous units separated by oblique and vertically oriented zones characterized by moderate-to-high V_P/V_S values (≥1.76, see Figure 7, Profile P19). This pattern may reflect a more fragmented and compositionally more mafic upper-plate crust. Such a configuration is compatible with a thinner crust, rarely exceeding 30–40 km, as also observed by Gao et al. (2025), which is consistent with previous studies on crustal composition and evolution of the central Andes (e.g., R. W. Kay & Mahlburg-Kay, 1991; S. M. Kay & Mpodozis, 2001; S. M. Kay et al., 1999).

In the shallow crust, the north-to-south traces of the Atacama Fault System (AFS) and the Domeyko Fault System (DFS) (Santibáñez et al., 2018) marked as "x" in Figures 4, 5, and 7 appear to roughly correlate with localized "V_P/V_S discontinuities" in the continental crust. Here, we refer to a "V_P/V_S discontinuity" as a lateral break or disruption in the otherwise continuous low-V_P/V_S (≤1.74) crustal domain, manifested as narrow zones with intermediate-to-elevated V_P/V_S ratios (≥1.76).

When taking these anomalies as proxies for the AFS and DFS, their observed shapes suggest contrasting crustal geometries for both fault systems. The AFS-related anomalies show limited crustal penetration, dip eastward, and extend to depths of only ∼20 km, consistent with previous studies (Amilibia et al., 2008; González et al., 2024; Pastén-Araya et al., 2018). In contrast, the DFS is interpreted as a broader rheological boundary, which dips westward, and extends to greater depths, in agreement with the tectonic evolutionary model of Amilibia et al. (2008) and recent geophysical observations (Bloch et al., 2014; Contreras-Reyes et al., 2021; Leon-Rios et al., 2024). Given that there is no current seismic activity along much of these fault zones recorded by our local experiment, these relationships should be considered with caution, and further high-resolution and active geophysical investigations are required to better constrain the connection between these ancient crustal structures and the observed V_P/V_S discontinuities within the shallower continental crust.

In a few localities along the traces of these fault systems, prominent clusters of seismicity spatially correlate with mining operations. The observed vertical distribution of seismicity is explained by the sequence of explosions used in mining, which generates reduced and unclear S-wave arrivals, resulting in poor constraints for hypocentral depths. These mining locations, denoted by black "Y" symbols in Figures 4, 5, and 7, correspond to recognized major mining sites. These zones also show a clear correlation with anomalous V_P/V_S ratios in the

uppermost crust, with V_P/V_S values ranging from 1.70 to 1.90. This suggests a link between the shallow anomalous V_P/V_S zones and different ore types being mined. Specifically, low V_P/V_S ratios are associated with open-pit iron ore operations (e.g., Mina Los Colorados, Mina El Pleito) and large porphyry copper (Cu-Mo) deposits (e.g., Mina Candelaria), consistent with the findings of Comte et al. (2023). In contrast, higher V_P/V_S values are linked to smaller-scale mining sites targeting mineralized oxide copper zones (e.g., Mina Doña Elba) and areas with extraction of carbonate-rich minerals (e.g., Mina Jilguero). These spatial correlations indicate that studies of regional seismic wavespeed anomalies could help to improve the recognition of large-scale ore structures.

7. Conclusions

This study presents a high-resolution seismic tomography model for the Atacama subduction zone, derived from over 8,800 earthquakes detected during approximately 18 months of observations from a dense temporary seismic network in North-Central Chile. The results reveal several features of the continental crust and downgoing oceanic slab, providing new insights into fluid migration and crustal heterogeneity in this tectonically active region, complementing previous seismic studies that were more limited in terms of network geometry, spatial coverage, and resolution over the past decades. Overall, our results are broadly consistent with previous regional and local tomography studies (Gao et al., 2025; Klein et al., 2021; Leon-Rios et al., 2024; Pastén-Araya et al., 2022), which similarly image a coherent high-V_P oceanic slab and elevated V_P/V_S ratios along the plate interface. Differences between models likely reflect differences in network geometry, resolution, and starting velocity models. In particular, the dense local network used here allows the resolution of smaller-scale structures compared to most previous studies.

A novel slab surface model, inferred from relocated seismicity, reveals significant differences from previous models, such as SLAB2, offering an improved understanding of the interplate contact obtained through our local observations. The downgoing Nazca Plate shows a characteristic V_P structure with low crustal velocities ($V_P \leq 7.8$) at the top, indicative of hydrated oceanic crust, transitioning into high-V_P ($V_P \geq 8.0$) material deeper in the slab. Elevated V_P/V_S ratios ($\geq$1.82) observed in the uppermost layer of the oceanic slab suggest fluid release during subduction, with clear associations to intermediate-depth seismicity. These findings are consistent with a link between dehydration processes and intraslab seismicity at different depths, suggesting that fluid migration may play a key role in deep seismic activity.

Around the subduction of the Copiapó Ridge, we found that oceanic features may promote fluid transport, enhancing localized fluid content and facilitating fluid migration along permeable pathways. This process may contribute to conditions favorable for slow slip events (SSEs), both at shallow depth and below the mantle wedge, reinforcing the link between fluid content and seismic behavior. In particular, our findings of a low V_P/V_S anomaly ($\leq$1.74) in the updip portion of the SSE, followed by higher V_P/V_S ratios ($\geq$ 1.80) in the downdip region, suggest substantial variations in fluid content. These variations may be linked to fluid migration during an inter-slip period or to doming structures acting as barriers to fluid ascent.

While both V_P/V_S and V_P provide insight into the relationship between seismic structure and interplate locking, along-dip variations show stronger and more consistent spatial correlations. These include the apparent control of elevated V_P/V_S ratios ($\geq$1.82), negative ΔV_P anomalies (with respect to the 1D V_P model), and low V_P values ($\leq$6.8 km/s) on the downdip extent of highly locked zones ($\geq$0.7). Along-strike relationships are weaker, particularly for V_P/V_S, and may be reduced by resolution limitations offshore.

Our study also reveals significant variations in the thickness and structure of the continental crust. A 30–50 km thick crust in the north ($\sim$24.4°S–$\sim$26.6°S) lacks significant fluid penetration from the plate interface. In the south ($\sim$28.6°S–$\sim$29.8°S), the crust is thinner and more fragmented, with zones of weaker structures rising from the mantle wedge, some of which reach the shallow crust, where broad outcrops related to the DFS have been recognized. Additionally, shallow V_P/V_S anomalies in the upper crust correlate with known mining areas spatially.

This study demonstrates the utility of combining machine learning earthquake phase picking with high-resolution tomography to improve our understanding of fluid pathways, crustal structures, and the delineation of ore-rich areas, as well as their role in seismic processes along subduction zones.

Conflict of Interest

The authors declare no conflicts of interest relevant to this study.

Availability Statement

The seismic waveform data are available from the networks Y6 (Tilmann et al., 2021), XZ (Socquet et al., 2020), C1 (Universidad de Chile, 2012), CX (GFZ German Research Centre For Geosciences & Institut Des Sciences De L'Univers-Centre National De La Recherche CNRS-INSU, 2006), and IU (Albuquerque Seismological Laboratory/USGS, 1988). The data were downloaded from the EarthScope, EPOS-FR and GEOFON data centers. We used the VELEST (Kissling et al., 1994), SIMUL2023 (Eberhart-Phillips et al., 2024) and hypoDD (Waldhauser, 2001) software packages for 1D inversions, tomographic inversion and relative relocation. All results of the present manuscript (velocity models, relocated seismicity, slab surface) are provided in a Zenodo repository (Hernández-Soto et al., 2025).

Acknowledgments

N.H.S acknowledges partial funding and support from Programa Nacional de Becas de Postgrado (Grant D-21210575), from Agencia Nacional de Desarrollo e Investigacion (ANID) through grant ANILLO PRECURSOR (ACT192169), from the Dirección de Postgrados at Universidad de Concepción and from the ANID-CAS International networks Development and Mobility Plus program (FOVI220075). M.Mi. acknowledges the support of FONDECYT Project 11130355. M.Mo. acknowledges support from ICN12019N Instituto Millenio de Oceanografía and FONDECYT project 1221507. C.S. and A.S. have received funding from the European Research Council (ERC) under the European Union's Horizon 2020 research and innovation programme (ERC Starting Grant StG2020-947856 MILESTONE and ERC Consolidator Grant 865963 DEEP-trigger). The GFZ expedition fund provided funding for the deployment of the Y6 network, which was coordinated by Ben Heit and Marcos Moreno. We thank everyone involved in the deployment of the seismic and geodetic networks and the data management. We thank the GFZ Geophysical Instrument Pool Potsdam (GIPP) and the Epos-France Mobile Seismological equipment Specific Action (SA Sismob) for providing the seismological instruments used in this study. We thank the Epos-France, GEOFON and Earthscope data centers for making data available.

References

Albuquerque Seismological Laboratory/USGS. (1988). Global Seismograph Network (GSN - IRIS/USGS) [Dataset]. *International Federation of Digital Seismograph Networks*. https://doi.org/10.7914/SN/IU

Álvarez, O., Gimenez, M., Folguera, A., Spagnotto, S., Bustos, E., Baez, W., & Braitenberg, C. (2015). New evidence about the subduction of the Copiapó ridge beneath South America, and its connection with the Chilean-Pampean flat slab, tracked by satellite GOCE and EGM2008 models. *Journal of Geodynamics*, *91*, 65–88. https://doi.org/10.1016/j.jog.2015.08.002

Amilibia, A., Sàbat, F., McClay, K., Muñoz, J., Roca, E., & Chong, G. (2008). The role of inherited tectono-sedimentary architecture in the development of the central Andean mountain belt: Insights from the Cordillera de Domeyko. *Journal of Structural Geology*, *30*(12), 1520–1539. https://doi.org/10.1016/j.jsg.2008.08.005

Angermann, D., Klotz, J., & Reigber, C. (1999). Space-geodetic estimation of the Nazca-South America Euler vector. *Earth and Planetary Science Letters*, *171*(3), 329–334. https://doi.org/10.1016/s0012-821x(99)00173-9

Barnes, P. M., Lamarche, G., Bialas, J., Henrys, S., Pecher, I., Netzeband, G. L., et al. (2010). Tectonic and geological framework for gas hydrates and cold seeps on the Hikurangi subduction margin, New Zealand. *Marine Geology*, *272*(1–4), 26–48. https://doi.org/10.1016/j.margeo.2009.03.012

Barnes, P. M., Wallace, L. M., Saffer, D. M., Bell, R. E., Underwood, M. B., Fagereng, A., et al. (2020). Slow slip source characterized by lithological and geometric heterogeneity. *Science Advances*, *6*(13), eaay3314. https://doi.org/10.1126/sciadv.aay3314

Beck, S., Barrientos, S., Kausel, E., & Reyes, M. (1998). Source characteristics of historic earthquakes along the central Chile subduction Askew et Alzone. *Journal of South American Earth Sciences*, *11*(2), 115–129. https://doi.org/10.1016/S0895-9811(98)00005-4

Bello-González, J. P., Contreras-Reyes, E., & Arriagada, C. (2018). Predicted path for hotspot tracks off South America since Paleocene times: Tectonic implications of ridge-trench collision along the Andean margin. *Gondwana Research*, *64*, 216–234. https://doi.org/10.1016/j.gr.2018.07.008

Bloch, W., Kummerow, J., Salazar, P., Wigger, P., & Shapiro, S. A. (2014). High-resolution image of the North Chilean subduction zone: Seismicity, reflectivity and fluids. *Geophysical Journal International*, *197*(3), 1744–1749. https://doi.org/10.1093/gji/ggu084

Brudzinski, M. R., Thurber, C. H., Hacker, B. R., & Engdahl, E. R. (2007). Global prevalence of double benioff zones. *Science*, *316*(5830), 1472–1474. https://doi.org/10.1126/science.1139204

Christensen, N. I. (1996). Poisson's ratio and crustal seismology. *Journal of Geophysical Research*, *101*(B2), 3139–3156. https://doi.org/10.1029/95jb03446

Christensen, N. I. (2004). Serpentinites, peridotites, and seismology. *International Geology Review*, *46*(9), 795–816. https://doi.org/10.2747/0020-6814.46.9.795

Christeson, G. L., Goff, J. A., & Reece, R. S. (2019). Synthesis of oceanic crustal structure from two-dimensional seismic profiles. *Reviews of Geophysics*, *57*(2), 504–529. https://doi.org/10.1029/2019RG000641

Comte, D., Haessler, H., Dorbath, L., Pardo, M., Monfret, T., Lavenu, A., et al. (2002). Seismicity and stress distribution in the Copiapo, northern Chile subduction zone using combined on-and off-shore seismic observations. *Physics of the Earth and Planetary Interiors*, *132*(1–3), 197–217. https://doi.org/10.1016/s0031-9201(02)00052-3

Comte, D., Palma, G., Vargas, J., Calle-Gardella, D., Peña, M., García-Fierro, S., et al. (2023). Imaging the subsurface architecture in porphyry copper deposits using local earthquake tomography. *Scientific Reports*, *13*(1), 6812. https://doi.org/10.1038/s41598-023-33820-w

Contreras-Reyes, E., & Carrizo, D. (2011). Control of high oceanic features and subduction channel on earthquake ruptures along the Chile–Peru subduction zone. *Physics of the Earth and Planetary Interiors*, *186*(1–2), 49–58. https://doi.org/10.1016/j.pepi.2011.03.002

Contreras-Reyes, E., Díaz, D., Bello-González, J., Slezak, K., Potin, B., Comte, D., et al. (2021). Subduction zone fluids and arc magmas conducted by lithospheric deformed regions beneath the central Andes. *Scientific Reports*, *11*(1), 1–12. https://doi.org/10.1038/s41598-021-02430-9

Cortés-Aranda, J., González, J., Molina, D., Astudillo-Sotomayor, L., Tassara, A., Miller, M., et al. (2022). Linking upper-plate fault reactivation with the megathrust earthquake cycle: The case of the northern Chile outer forearc (19°S–23°S). *Tectonics*, *41*(11), e2021TC006956. https://doi.org/10.1029/2021tc006956

DeMets, C., Gordon, R. G., & Argus, D. F. (2010). Geologically current plate motions. *Geophysical Journal International*, *181*(1), 1–80. https://doi.org/10.1111/j.1365-246x.2009.04491.x

Dorbath, C., Gerbault, M., Carlier, G., & Guiraud, M. (2008). Double seismic zone of the Nazca plate in northern Chile: High-resolution velocity structure, petrological implications, and thermomechanical modeling. *Geochemistry, Geophysics, Geosystems*, *9*(7), Q07006. https://doi.org/10.1029/2008GC002020

Eberhart-Phillips, D. (1986). Three-dimensional velocity structure in northern California Coast Ranges from inversion of local earthquake arrival times. *Bulletin of the Seismological Society of America*, *76*(4), 1025–1052.

Eberhart-Phillips, D., & Michael, A. J. (1998). Seismotectonics of the Loma Prieta, California, region determined from three-dimensional Vp, Vp/Vs, and seismicity. *Journal of Geophysical Research*, *103*(B9), 21099–21120.

Eberhart-Phillips, D., Thurber, C., Rietbrock, A., Fry, B., Reyners, M., & Lanza, F. (2024). Simul2023: A flexible program for inversion of earthquake data for 3-D velocity and hypocenters or 3-D Q [Software]. *Zenodo*. https://doi.org/10.5281/zenodo.10695070

Faccenda, M. (2014). Water in the slab: A trilogy. *Tectonophysics*, *614*, 1–30. https://doi.org/10.1016/j.tecto.2013.12.020

Gao, L., Chen, Z., Liu, Y., Zhang, H., Hu, J., Comte, D., & Culaciati, F. H. O. (2025). High-resolution seismic tomography of the transition zone from normal to flat slab subduction in central Chile: Implications for volcanoes, plate coupling and flat subduction. *Earth and Planetary Science Letters*, *651*, 119167. https://doi.org/10.1016/j.epsl.2024.119167

Garth, T., & Rietbrock, A. (2017). Constraining the hydration of the subducting Nazca plate beneath Northern Chile using subduction zone guided waves. *Earth and Planetary Science Letters*, *474*, 237–247. https://doi.org/10.1016/j.epsl.2017.06.041

Gase, A. C., Bangs, N. L., Saffer, D. M., Han, S., Miller, P. K., Bell, R. E., et al. (2023). Subducting volcaniclastic-rich upper crust supplies fluids for shallow megathrust and slow slip. *Science Advances*, *9*(33), eadh0150. https://doi.org/10.1126/sciadv.adh0150

GEBCO Bathymetric Compilation Group. (2023). GEBCO 2023 Grid [Dataset]. *British Oceanographic Data Centre*. https://doi.org/10.5285/f98b053b-0cbc-6c23-e053-6c86abc0af7b

Geersen, J., Sippl, C., & Harmon, N. (2022). Impact of bending-related faulting and oceanic-plate topography on slab hydration and intermediate-depth seismicity. *Geosphere*, *18*(2), 562–584. https://doi.org/10.1130/ges02367.1

GFZ German Research Centre For Geosciences, & Institut Des Sciences De L'Univers-Centre National De La Recherche CNRS-INSU. (2006). IPOC seismic network [Dataset]. *Integrated Plate boundary Observatory Chile - IPOC*. https://doi.org/10.14470/PK615318

González, Y., González, G., Spagnuolo, E., Pozzi, G., Jensen, E., Aretusini, S., & Schleicher, A. M. (2024). Exploring frictional properties of upper plate fault reactivation in subduction zones: The Atacama Fault System in northern Chile. *Earth and Planetary Science Letters*, *648*, 119106. https://doi.org/10.1016/j.epsl.2024.119106

González-Vidal, D., Moreno, M., Sippl, C., Baez, J. C., Ortega-Culaciati, F., Lange, D., et al. (2023). Relation between oceanic plate structure, patterns of interplate locking and microseismicity in the 1922 Atacama seismic gap. *Geophysical Research Letters*, *50*(15), e2023GL103565. https://doi.org/10.1029/2023gl103565

Graeber, F. M., & Asch, G. (1999). Three-dimensional models of P wave velocity and *P*-to-*S* velocity ratio in the southern central Andes by simultaneous inversion of local earthquake data. *Journal of Geophysical Research*, *104*(B9), 20237–20256. https://doi.org/10.1029/1999JB900037

Grevemeyer, I., Ranero, C. R., & Ivandic, M. (2018). Structure of oceanic crust and serpentinization at subduction trenches. *Geosphere*, *14*(2), 395–418. https://doi.org/10.1130/GES01537.1

Haberland, C., Rietbrock, A., Lange, D., Bataille, K., & Dahm, T. (2009). Structure of the seismogenic zone of the southcentral Chilean margin revealed by local earthquake traveltime tomography. *Journal of Geophysical Research*, *114*(B1), B01317. https://doi.org/10.1029/2008jb005802

Hacker, B. R., Peacock, S. M., Abers, G. A., & Holloway, S. D. (2003). Subduction factory 2. Are intermediate-depth earthquakes in subducting slabs linked to metamorphic dehydration reactions? *Journal of Geophysical Research*, *108*(B1), 2030. https://doi.org/10.1029/2001jb001129

Hayes, G. P., Moore, G. L., Portner, D. E., Hearne, M., Flamme, H., Furtney, M., & Smoczyk, G. M. (2018). Slab2, a comprehensive subduction zone geometry model. *Science*, *362*(6410), 58–61. https://doi.org/10.1126/science.aat4723

Hernández-Soto, N., Sippl, C., Miller, M., Lange, D., Tilmann, F., González-Vidal, D., et al. (2025). Supporting materials for "Structure of the North-Central Chile subduction zone from local earthquake tomography" - Velocity models, relocated earthquake catalogs, and local slab surface data for the Atacama segment [Dataset]. *Zenodo*. https://doi.org/10.5281/zenodo.15641812

Hicks, S. P., Rietbrock, A., Ryder, I. M., Lee, C.-S., & Miller, M. (2014). Anatomy of a megathrust: The 2010 M8.8 Maule, Chile earthquake rupture zone imaged using seismic tomography. *Earth and Planetary Science Letters*, *405*, 142–155. https://doi.org/10.1016/j.epsl.2014.08.028

Holtkamp, S. G., Pritchard, M., & Lohman, R. (2011). Earthquake swarms in South America. *Geophysical Journal International*, *187*(1), 128–146. https://doi.org/10.1111/j.1365-246x.2011.05137.x

Husen, S., & Kissling, E. (2001). Postseismic fluid flow after the large subduction earthquake of Antofagasta, Chile. *Geology*, *29*(9), 847–850. https://doi.org/10.1130/0091-7613(2001)029<0847:pffatl>2.0.co;2

Husen, S., Kissling, E., Flueh, E., & Asch, G. (1999). Accurate hypocentre determination in the seismogenic zone of the subducting Nazca Plate in northern Chile using a combined on-/offshore network. *Geophysical Journal International*, *138*(3), 687–701. https://doi.org/10.1046/j.1365-246x.1999.00893.x

Husen, S., Kissling, E., & Flueh, E. R. (2000). Local earthquake tomography of shallow subduction in north Chile: A combined onshore and offshore study. *Journal of Geophysical Research*, *105*(B12), 28183–28198. https://doi.org/10.1029/2000jb900229

Hyndman, R. D., & Peacock, S. M. (2003). Serpentinization of the forearc mantle. *Earth and Planetary Science Letters*, *212*(3–4), 417–432. https://doi.org/10.1016/s0012-821x(03)00263-2

Kato, A., Iidaka, T., Ikuta, R., Yoshida, Y., Katsumata, K., Iwasaki, T., et al. (2010). Variations of fluid pressure within the subducting oceanic crust and slow earthquakes. *Geophysical Research Letters*, *37*(14), L14310. https://doi.org/10.1029/2010gl043723

Kay, R. W., & Mahlburg-Kay, S. (1991). Creation and destruction of lower continental crust. *Geologische Rundschau*, *80*(2), 259–278. https://doi.org/10.1007/BF01829365

Kay, S. M., & Mpodozis, C. (2001). Central Andean Ore deposits linked to evolving shallow subduction systems and thickening crust. [Article]. *Geological Society of America Today*, *11*(3), 4–9. https://doi.org/10.1130/1052-5173(2001)011⟨0004:CAODLT⟩2.0.CO;2

Kay, S. M., Mpodozis, C., & Coira, B. (1999). Neogene Magmatism, Tectonism, and Mineral Deposits of the Central Ande (22° to 33°S Latitude). In *Geology and ore deposits of the central andes*. Society of Economic Geologists. https://doi.org/10.5382/SP.07.02

Kirby, S. H., Stein, S., Okal, E. A., & Rubie, D. C. (1996). Metastable mantle phase transformations and deep earthquakes in subducting oceanic lithosphere. *Reviews of Geophysics*, *34*(2), 261–306. https://doi.org/10.1029/96rg01050

Kissling, E., Ellsworth, W., Eberhart-Phillips, D., & Kradolfer, U. (1994). Initial reference models in local earthquake tomography [Software]. *Journal of Geophysical Research*, *99*(B10), 19635–19646. https://doi.org/10.1029/93JB03138

Klein, E., Duputel, Z., Zigone, D., Vigny, C., Boy, J.-P., Doubre, C., & Meneses, G. (2018). Deep transient slow slip detected by survey GPS in the Region of Atacama, Chile. *Geophysical Research Letters*, *45*(22), 12263–12273. https://doi.org/10.1029/2018GL080613

Klein, E., Metois, M., Meneses, G., Vigny, C., & Delorme, A. (2018). Bridging the gap between North and Central Chile: Insight from new GPS data on coupling complexities and the Andean sliver motion. *Geophysical Journal International*, *213*(3), 1924–1933. https://doi.org/10.1093/gji/ggy094

Klein, E., Potin, B., Pasten-Araya, F., Tissandier, R., Azua, K., Duputel, Z., et al. (2021). Interplay of seismic and a-seismic deformation during the 2020 sequence of Atacama, Chile. *Earth and Planetary Science Letters*, *570*, 117081. https://doi.org/10.1016/j.epsl.2021.117081

Klein, E., Vigny, C., Duputel, Z., Zigone, D., Rivera, L., Ruiz, S., & Potin, B. (2023). Return of the Atacama deep slow slip event: The 5-year recurrence confirmed by continuous GPS. *Physics of the Earth and Planetary Interiors*, *334*, 106970. https://doi.org/10.1016/j.pepi.2022.106970

Kodaira, S., Iidaka, T., Kato, A., Park, J.-O., Iwasaki, T., & Kaneda, Y. (2004). High pore fluid pressure may cause silent slip in the Nankai Trough. *Science*, *304*(5675), 1295–1298. https://doi.org/10.1126/science.1096535

Korenaga, J. (2017). On the extent of mantle hydration caused by plate bending. *Earth and Planetary Science Letters*, *457*, 1–9. https://doi.org/10.1016/j.epsl.2016.10.011

Koulakov, I. (2009). Out-of-network events can be of great importance for improving results of local earthquake tomography. *Bulletin of the Seismological Society of America*, *99*(4), 2556–2563. https://doi.org/10.1785/0120080365

Koulakov, I., Sobolev, S. V., & Asch, G. (2006). P-and S-velocity images of the lithosphere—asthenosphere system in the Central Andes from local-source tomographic inversion. *Geophysical Journal International*, *167*(1), 106–126. https://doi.org/10.1111/j.1365-246x.2006.02949.x

Kukowski, N., & Oncken, O. (2006). Subduction erosion—The "normal" mode of fore-arc material transfer along the Chilean margin? In *The Andes: Active Subduction Orogeny* (pp. 217–236). Springer.

Lange, D., Tilmann, F., Henstock, T., Rietbrock, A., Natawidjaja, D., & Kopp, H. (2018). Structure of the central Sumatran subduction zone revealed by local earthquake travel-time tomography using an amphibious network. *Solid Earth*, *9*(4), 1035–1049. https://doi.org/10.5194/se-9-1035-2018

Leon-Rios, S., Reyes-Wagner, V., Calle-Gardella, D., Rietbrock, A., Roecker, S., Maksymowicz, A., & Comte, D. (2024). Structural characterization of the Taltal segment in Northern Chile between 22°S and 26°S using local earthquake tomography. *Geochemistry, Geophysics, Geosystems*, *25*(5), e2023GC011197. https://doi.org/10.1029/2023gc011197

Ma, B., Geersen, J., Lange, D., Klaeschen, D., Grevemeyer, I., Contreras-Reyes, E., et al. (2022). Megathrust reflectivity reveals the updip limit of the 2014 Iquique earthquake rupture. *Nature Communications*, *13*(1), 3969. https://doi.org/10.1038/s41467-022-31448-4

Marsan, D., Reverso, T., & Socquet, A. (2023). Earthquake swarms along the Chilean subduction zone, 2003–2020. *Geophysical Journal International*, *235*(3), 2758–2777. https://doi.org/10.1093/gji/ggad359

Metcalf, K., & Kapp, P. (2015). Along-strike variations in crustal seismicity and modern lithospheric structure of the central Andean forearc. In *Geodynamics of a Cordilleran Orogenic System: The Central Andes of Argentina and Northern Chile*. Geological Society of America. https://doi.org/10.1130/2015.1212(04)

Metois, M., Vigny, C., & Socquet, A. (2016). Interseismic coupling, megathrust earthquakes and seismic swarms along the Chilean subduction zone (38°–18°S). *Pure and Applied Geophysics*, *173*(5), 1431–1449. https://doi.org/10.1007/s00024-016-1280-5

Métois, M., Vigny, C., Socquet, A., Delorme, A., Morvan, S., Ortega, I., & Valderas-Bermejo, C.-M. (2014). GPS-derived interseismic coupling on the subduction and seismic hazards in the Atacama region, Chile. *Geophysical Journal International*, *196*(2), 644–655. https://doi.org/10.1093/gji/ggt418

Mishra, O., Zhao, D., Umino, N., & Hasegawa, A. (2003). Tomography of northeast Japan forearc and its implications for interplate seismic coupling. *Geophysical Research Letters*, *30*(16), 1850. https://doi.org/10.1029/2003gl017736

Molina, D., Tassara, A., Abarca, R., Melnick, D., & Madella, A. (2020). Frictional segmentation of the Chilean megathrust from a multivariate analysis of geophysical, geological and geodetic data. *Journal of Geophysical Research: Solid Earth*, *126*(6), e2020JB020647. https://doi.org/10.1029/2020jb020647

Molina-Ormazabal, D., Radiguet, M., Münchmeyer, J., Hernández-Soto, N., Vezinet, A., Pousse-Beltran, L., et al. (2025). Slip modes along a structurally-driven earthquake barrier in Chile. *Journal of Geophysical Research: Solid Earth*, *130*(6), e2024JB030796. https://doi.org/10.1029/2024JB030796

Mooney, W. (2007). Crust and lithospheric structure – Global crustal structure. In G. Schubert (Ed.), *Treatise on geophysics* (pp. 361–417). Elsevier. https://doi.org/10.1016/B978-044452748-6.00011-0

Mooney, W. D., Barrera-Lopez, C., Suárez, M. G., & Castelblanco, M. A. (2023). Earth Crustal Model 1 (ECM1): A 1° × 1° Global Seismic and Density Model. *Earth-Science Reviews*, *243*, 104493. https://doi.org/10.1016/j.earscirev.2023.104493

Mooney, W. D., Barrera-Lopez, P., & Suárez, M. G. (2025). Secular evolution of the seismic structure of continental crust, Archean to present. *Journal of Geophysical Research: Solid Earth*, *130*(10), e2025JB031907. https://doi.org/10.1029/2025jb031907

Moreno, M., Haberland, C., Oncken, O., Rietbrock, A., Angiboust, S., & Heidbach, O. (2014). Locking of the Chile subduction zone controlled by fluid pressure before the 2010 earthquake. *Nature Geoscience*, *7*(4), 292–296. https://doi.org/10.1038/ngeo2102

Mousavi, S. M., Ellsworth, W. L., Zhu, W., Chuang, L. Y., & Beroza, G. C. (2020). Earthquake transformer—An attentive deep-learning model for simultaneous earthquake detection and phase picking. *Nature Communications*, *11*(1), 3952. https://doi.org/10.1038/s41467-020-17591-w

Müller, R. D., Zahirovic, S., Williams, S. E., Cannon, J., Seton, M., Bower, D. J., et al. (2019). A global plate model including lithospheric deformation along major rifts and orogens since the Triassic. *Tectonics*, *38*(6), 1884–1907. https://doi.org/10.1029/2018TC005462

Münchmeyer, J. (2024). PyOcto: A high-throughput seismic phase associator. *Seismica*, *3*(1). https://doi.org/10.26443/seismica.v3i1.1130

Münchmeyer, J., Frank, W. B., Giffard-Roisin, S., Marsan, D., & Socquet, A. (2025). A systematic search for tectonic tremor and low-frequency earthquakes in the Atacama segment of the Chilean subduction zone (24°S–31°S) turns up empty. https://arxiv.org/abs/2501.16934

Münchmeyer, J., Molina-Ormazabal, D., Marsan, D., Langlais, M., Baez, J.-C., Heit, B., et al. (2025). Characterizing the Atacama segment of the Chile subduction margin (24°S–31°S) with >165,000 earthquakes. *Journal of Geophysical Research: Solid Earth*, *130*(7), e2025JB031256. https://doi.org/10.1029/2025JB031256

Münchmeyer, J., Molina-Ormazabal, D., Radiguet, M., Marsan, D., Baez, J.-C., Ortega-Culaciati, F., et al. (2025). Seismic swarms unveil the mechanisms driving shallow slow slip dynamics in the Copiapó ridge, Northern Chile. *Geophysical Research Letters*, *52*(8), e2024GL113953. https://doi.org/10.1029/2024gl113953

Münchmeyer, J., Woollam, J., Rietbrock, A., Tilmann, F., Lange, D., Bornstein, T., et al. (2022). Which picker fits my data? A quantitative evaluation of deep learning based seismic pickers. *Journal of Geophysical Research: Solid Earth*, *127*(1), e2021JB023499. https://doi.org/10.1029/2021jb023499

Nakajima, J., & Uchida, N. (2018). Repeated drainage from megathrusts during episodic slow slip. *Nature Geoscience*, *11*(5), 351–356. https://doi.org/10.1038/s41561-018-0090-z

Nishikawa, T., & Ide, S. (2017). Detection of earthquake swarms at subduction zones globally: Insights into tectonic controls on swarm activity. *Journal of Geophysical Research: Solid Earth*, *122*(7), 5325–5343. https://doi.org/10.1002/2017jb014188

Ojeda, J., Morales-Yáñez, C., Ducret, G., Ruiz, S., Grandin, R., Doin, M.-P., et al. (2023). Seismic and aseismic slip during the 2006 Copiapó swarm in North-Central Chile. *Journal of South American Earth Sciences*, *123*, 104198. https://doi.org/10.1016/j.jsames.2023.104198

Oliveros, V., Morata, D., Aguirre, L., Féraud, G., & Fornari, M. (2007). Magmatismo asociado a subducción del Jurásico a Cretácico Inferior en la Cordillera de la Costa del norte de Chile (18° 30′–24°S): Geoquímica y petrogenesis. *Revista Geologica de Chile*, *34*(2), 209–232. https://doi.org/10.5027/andgeov34n2-a03

Pastén-Araya, F., Potin, B., Azua, K., Saez, M., Aden-Antoniów, F., Ruiz, S., et al. (2022). Along-dip segmentation of the slip behavior and rheology of the Copiapó ridge subducted in North-Central Chile. *Geophysical Research Letters*, *49*(4), e2021GL095471. https://doi.org/10.1029/2021gl095471

Pastén-Araya, F., Salazar, P., Ruiz, S., Rivera, E., Potin, B., Maksymowicz, A., et al. (2018). Fluids along the plate interface influencing the frictional regime of the Chilean subduction zone, northern Chile. *Geophysical Research Letters*, *45*(19), 10–378. https://doi.org/10.1029/2018gl079283

Patzwahl, R., Mechie, J., Schulze, A., & Giese, P. (1999). Two-dimensional velocity models of the Nazca plate subduction zone between 19.5°S and 25°S from wide-angle seismic measurements during the CINCA95 project. *Journal of Geophysical Research*, *104*(B4), 7293–7317. https://doi.org/10.1029/1999jb900008

Peacock, S. M. (2001). Are the lower planes of double seismic zones caused by serpentine dehydration in subducting oceanic mantle? *Geology*, *29*(4), 299–302. https://doi.org/10.1130/0091-7613(2001)029<0299:atlpod>2.0.co;2

Potin, B., Ruiz, S., Aden-Antoniow, F., Madariaga, R., & Barrientos, S. (2025). A revised Chilean seismic catalog from 1982 to mid-2020. *Seismological Research Letters*, *96*(1), 484–498. https://doi.org/10.1785/0220240047

Puente Huerta, J., Sippl, C., Münchmeyer, J., & McBrearty, I. W. (2025). Benchmarking seismic phase associators: Insights from synthetic scenarios. *Seismica*, *4*(2). https://doi.org/10.26443/seismica.v4i2.1559

Ramos, V. A., Cristallini, E. O., & Pérez, D. J. (2002). The Pampean flat-slab of the Central Andes. *Journal of South American Earth Sciences*, *15*(1), 59–78. https://doi.org/10.1016/s0895-9811(02)00006-8

Ranero, C. R., Phipps Morgan, J., McIntosh, K., & Reichert, C. (2003). Bending-related faulting and mantle serpentinization at the Middle America trench. *Nature*, *425*(6956), 367–373. https://doi.org/10.1038/nature01961

Ranero, C. R., & Sallarès, V. (2004). Geophysical evidence for hydration of the crust and mantle of the Nazca plate during bending at the north Chile trench. *Geology*, *32*(7), 549–552. https://doi.org/10.1130/g20379.1

Ruegg, J. C., Campos, J., Armijo, R., Barrientos, S., Briole, P., Thiele, R., et al. (1996). The Mw=8.1 Antofagasta (North Chile) Earthquake of July 30, 1995: First results from teleseismic and geodetic data. *Geophysical Research Letters*, *23*(9), 917–920. https://doi.org/10.1029/96GL01026

Ruiz, S., & Madariaga, R. (2018). Historical and recent large megathrust earthquakes in Chile. *Tectonophysics*, *733*, 37–56. https://doi.org/10.1016/j.tecto.2018.01.015

Rüpke, L. H., Morgan, J. P., Hort, M., & Connolly, J. A. (2004). Serpentine and the subduction zone water cycle. *Earth and Planetary Science Letters*, *223*(1–2), 17–34. https://doi.org/10.1016/j.epsl.2004.04.018

Sallarès, V., & Ranero, C. R. (2005). Structure and tectonics of the erosional convergent margin off Antofagasta, north Chile (23°30′S). *Journal of Geophysical Research*, *110*(B6), B06101. https://doi.org/10.1029/2004JB003418

Santibáñez, I., Cembrano, J., García-Pérez, T., Costa, C., Yáñez, G., Marquardt, C., et al. (2018). Crustal faults in the Chilean Andes: Geological constraints and seismic potential. *Andean Geology*, *46*(1), 32–65. https://doi.org/10.5027/andgeov46n1-3067

Schmalzle, G. M., McCaffrey, R., & Creager, K. C. (2014). Central Cascadia subduction zone creep. *Geochemistry, Geophysics, Geosystems*, *15*(4), 1515–1532. https://doi.org/10.1002/2013gc005172

Scholz, C. H. (1998). Earthquakes and friction laws. *Nature*, *391*(6662), 37–42. https://doi.org/10.1038/34097

Seton, M., Müller, R. D., Zahirovic, S., Williams, S., Wright, N. M., Cannon, J., et al. (2020). A global data set of present-day oceanic crustal age and seafloor spreading parameters. *Geochemistry, Geophysics, Geosystems*, *21*(10), e2020GC009214. https://doi.org/10.1029/2020GC009214

Shelly, D. R., Beroza, G. C., Ide, S., & Nakamula, S. (2006). Low-frequency earthquakes in Shikoku, Japan, and their relationship to episodic tremor and slip. *Nature*, *442*(7099), 188–191. https://doi.org/10.1038/nature04931

Shreedharan, S., Ikari, M., Wood, C., Saffer, D., Wallace, L., & Marone, C. (2022). Frictional and lithological controls on shallow slow slip at the northern Hikurangi margin. *Geochemistry, Geophysics, Geosystems*, *23*(2), e2021GC010107. https://doi.org/10.1029/2021gc010107

Shreedharan, S., Saffer, D., Wallace, L. M., & Williams, C. (2023). Ultralow frictional healing explains recurring slow slip events. *Science*, *379*(6633), 712–717. https://doi.org/10.1126/science.adf4930

Sippl, C., Schurr, B., Asch, G., & Kummerow, J. (2018). Seismicity structure of the northern Chile forearc from >100,000 double-difference relocated hypocenters. *Journal of Geophysical Research*, *123*(5), 4063–4087. https://doi.org/10.1002/2017JB015384

Sippl, C., Schurr, B., Tympel, J., Angiboust, S., Mechie, J., Yuan, X., et al. (2013). Deep burial of Asian continental crust beneath the Pamir imaged with local earthquake tomography. *Earth and Planetary Science Letters*, *384*, 165–177. https://doi.org/10.1016/j.epsl.2013.10.013

Sociedad Nacional de Minería. (2023). Mapa Minero de Chile. Retrieved from https://www.sonami.cl/mapaminero/

Socquet, A., Baez, J. C., Moreno, M., Langlais, M., & DEEP-Trigger Team, Geophysics Technical Service At ISTerre, & RESIF. (2020). Deep_trigger temporary experiment in the subduction zone Peru/Chile, Chile (Resif-Sismob) [Dataset]. *RESIF - Réseau Sismologique et géodésique Français*. https://doi.org/10.15778/RESIF.XZ2020

Sodoudi, F., Yuan, X., Asch, G., & Kind, R. (2011). High-resolution image of the geometry and thickness of the subducting Nazca lithosphere beneath northern Chile. *Journal of Geophysical Research*, *116*(B4), B04302. https://doi.org/10.1029/2010JB007829

Sparkes, R., Tilmann, F., Hovius, N., & Hillier, J. (2010). Subducted seafloor relief stops rupture in South American great earthquakes: Implications for rupture behaviour in the 2010 Maule, Chile earthquake. *Earth and Planetary Science Letters*, *298*(1–2), 89–94. https://doi.org/10.1016/j.epsl.2010.07.029

Tassara, A., & Echaurren, A. (2012). Anatomy of the Andean subduction zone: Three-dimensional density model upgraded and compared against global-scale models. *Geophysical Journal International*, *189*(1), 161–168. https://doi.org/10.1111/j.1365-246X.2012.05397.x

Tatsumi, Y. (1989). Migration of fluid phases and genesis of basalt magmas in subduction zones. *Journal of Geophysical Research*, *94*(B4), 4697–4707. https://doi.org/10.1029/jb094ib04p04697

Thurber, C., & Eberhart-Phillips, D. (1999). Local earthquake tomography with flexible gridding. *Computers & Geosciences*, *25*(7), 809–818. https://doi.org/10.1016/s0098-3004(99)00007-2

Tilmann, F., Heit, B., Moreno, M., & González-Vidal, D. (2021). Anillo [Dataset]. *GFZ Data Services*. https://doi.org/10.14470/L17575324477

Toomey, D., & Foulger, G. (1989). Tomographic inversion of local earthquake data from the Hengill-Grensdalur central volcano complex, Iceland. *Journal of Geophysical Research*, *94*(B12), 17497–17510. https://doi.org/10.1029/jb094ib12p17497

Tsuji, Y., Nakajima, J., & Hasegawa, A. (2008). Tomographic evidence for hydrated oceanic crust of the Pacific slab beneath northeastern Japan: Implications for water transportation in subduction zones. *Geophysical Research Letters*, *35*(14), L14308. https://doi.org/10.1029/2008gl034461

Um, J., & Thurber, C. (1987). A fast algorithm for two-point seismic ray tracing. *Bulletin of the Seismological Society of America*, *77*(3), 972–986. https://doi.org/10.1785/bssa0770030972

Universidad de Chile. (2012). Red Sismologica Nacional [Dataset]. *International Federation of Digital Seismograph Networks*. https://doi.org/10.7914/SN/C1

van Keken, P. E., Hacker, B. R., Syracuse, E. M., & Abers, G. A. (2011). Subduction factory: 4. Depth-dependent flux of H_2O from subducting slabs worldwide. *Journal of Geophysical Research*, *116*(B1), B01401. https://doi.org/10.1029/2010JB007922

Vigny, C., Klein, E., & Ojeda, J. (2024). In search for the lost truth about the 1922 & 1918 Atacama earthquakes in Chile. *Journal of South American Earth Sciences*, *143*, 104983.

von Huene, R., & Ranero, C. R. (2003). Subduction erosion and basal friction along the sediment-starved convergent margin off Antofagasta, Chile. *Journal of Geophysical Research*, *108*(B2), 2079. https://doi.org/10.1029/2001JB001569

Waldhauser, F. (2001). hypoDD—A program to compute double-difference hypocenter locations (hypoDD version 1.0-03/2001) [Software]. *US Geological Survey Open File Report, 01*, 113. Retrieved from https://www.ldeo.columbia.edu/~felixw/hypoDD.html

Waldhauser, F., & Ellsworth, W. L. (2000). A double-difference earthquake location algorithm: Method and application to the northern Hayward fault, California. *Bulletin of the Seismological Society of America*, *90*(6), 1353–1368. https://doi.org/10.1785/0120000006

Wallace, L. M. (2020). Slow slip events in New Zealand. *Annual Review of Earth and Planetary Sciences*, *48*(1), 175–203. https://doi.org/10.1146/annurev-earth-071719-055104

Wang, J., Xiao, Z., Liu, C., Zhao, D., & Yao, Z. (2019). Deep learning for picking seismic arrival times. *Journal of Geophysical Research: Solid Earth*, *124*(7), 6612–6624. https://doi.org/10.1029/2019jb017536

Warwel, A., Lange, D., Dannowski, A., Contreras-Reyes, E., Klaucke, I., Diaz-Naveas, J., et al. (2025). Seismic structure and tectonics of the North-Central Chilean subduction zone along the Copiapó Ridge from amphibious seismic refraction tomography and local seismicity. *Geochemistry, Geophysics, Geosystems*, *26*(1), e2024GC011829. https://doi.org/10.1029/2024GC011829

Warwel, A., Lange, D., Dannowski, A., Klaucke, I., Contreras-Reyes, E., Moreno, M., et al. (2025). Fault-induced hydration and serpentinization of the incoming lithosphere enhances intra-slab seismicity offshore Taltal (~25°S), Northern Chile. *Journal of Geophysical Research: Solid Earth*, *130*(12), e2025JB032891. https://doi.org/10.1029/2025JB032891

Woollam, J., Münchmeyer, J., Tilmann, F., Rietbrock, A., Lange, D., Bornstein, T., et al. (2022). SeisBench—A toolbox for machine learning in seismology. *Seismological Society of America*, *93*(3), 1695–1709. https://doi.org/10.1785/0220210324

Worthington, J. R., Hacker, B. R., & Zandt, G. (2013). Distinguishing eclogite from peridotite: EBSD-based calculations of seismic velocities. *Geophysical Journal International*, *193*(1), 489–505. https://doi.org/10.1093/gji/ggt004

Yuan, X., Sobolev, S. V., Kind, R., Oncken, O., Bock, G., Asch, G., et al. (2000). Subduction and collision processes in the Central Andes constrained by converted seismic phases. *Nature*, *408*(6815), 958–961. https://doi.org/10.1038/35050073

Zhan, Z. (2020). Mechanisms and implications of deep earthquakes. *Annual Review of Earth and Planetary Sciences*, *48*(1), 147–174. https://doi.org/10.1146/annurev-earth-053018-060314